Land Remote Sensing Applications Using Spaceborne GNSS Reflectometry: A Comprehensive Overview

Jinwei Bu, *Member, IEEE*, Qiulan Wang, Ziyi Wang, Shaoqiang Fan, Xinyu Liu, and Xiaoqing Zuo

***Abstract*—The refracted, reflected, and scattered signals from global navigation satellite systems (GNSSs) have been successfully used for remote sensing (RS) of the Earth's surface and atmosphere, demonstrating their potential for sensing the atmosphere, oceans, land surface and cryosphere. As an emerging RS technology, spaceborne GNSS reflectometry (GNSS-R) has been widely used in the field of land RS, with unique advantages such as high spatial and temporal resolution, low observation cost, wide coverage, and all-weather operation. In recent years, the successful launch of several spaceborne GNSS-R satellites has opened new opportunities in this field. The aim of this article is to provide a comprehensive overview of the breakthrough applications of spaceborne GNSS-R technology in the key areas of soil moisture, soil salinity, vegetation monitoring, soil freezing and thawing, flood detection, inland water bodies, wetland dynamics, forest fire disturbances, and land topography measurements, as well as possible future research directions. In addition, this article also emphasizes the contribution and role of China's recently launched Tianmu-1 constellation (as of 5 January 2024, 23 satellites have been in stable operation in orbit) in the development of spaceborne GNSS-R technology and explores the future development direction and prospects of this technology. By comprehensively analyzing the latest progress and innovative achievements of relevant research, the significant impact of this technology on land RS applications in environmental monitoring, resource management, and disaster warning has been highlighted. Through a comprehensive summary of these fields, the enormous potential of spaceborne GNSS-R technology in promoting sustainable development and ecological protection has been revealed.**

***Index Terms*—Disaster warning, ecological protection, environmental monitoring, land remote sensing (RS), resource management, spaceborne GNSS reflectometry (GNSS-R), Tianmu-1 (TM-1).**

I. Introduction

GLOBAL navigation satellite system reflectometry (GNSS-R), as an emerging remote sensing (RS) technology, has been a popular technology in the fields of ocean, land, atmosphere, and cryosphere RS in recent years. GNSS-R has shown enormous potential due to its advantages such as short revisit cycles and low observation costs. In 1988, Hall and Cordey [1] proposed the concept of GNSS bistatic radar. In 1993, Martin-Neira [2] first proposed the idea of using GNSS reflection signals for ocean altimetry. In 2003, the U.K. National Space Center launched the first U.K.-DMC satellite equipped with a global positioning system reflectometry (GPS-R) receiver and used it to receive and process GPS L1 C/A code reflection signals, verifying the feasibility of estimating sea surface wind speed, detecting sea ice, and retrieving other parameters on the spaceborne platform [3]. Then, in July 2014, a technology demonstration GNSS-R satellite TechDemoSat-1 (TDS-1) equipped with a space GPS receiver RS instrument was launched and operated for 4.5 years, collecting valuable in orbit data on sea surface wind, sea surface height, inland soil moisture (SM), and sea ice. The results of TDS-1 provide strong support for the future application of GNSS-R in global sea surface wind speed retrieval and sea ice detection [4], [5]. In December 2016, the National Aeronautics and Space Administration (NASA) launched the Cyclone GNSS (CYGNSS) mission [6], [7], [8], which consisted of eight microsatellites for observing tropical cyclones at high spatial and temporal resolutions. The CYGNSS mission successfully demonstrated the ability of GNSS-R technology to perceive tropical cyclone eyes at high temporal resolution, optimize tropical cyclone forecasts, provide monthly high-resolution SM products, and map inland water bodies. In the same year, the Universitat Politècnica de Catalunya launched their advanced spaceborne CubeSats with GNSS-R instruments called ^{3}Cat-2 mission [9]. In 2020, an improved version of ^{3}Cat-2 was developed and launched by the FSSCat mission (^{3}Cat-5/A and ^{3}Cat-5/B) sponsored by the European Space Agency (ESA) [10]. Spire CubeSats have also been successfully launched since 2019 [11], [12], [13]. In addition, the Chinese spaceborne GNSS-R era began with the BuFeng-1 (BF-1) mission in 2019, which was developed by the China Aerospace Science and Technology Corporation and launched by the Chinese first-time sea platform [14], [15], [16]. Since July 2021, China has also launched FengYun-3E/3F/3G (FY-3E/3F/3G) and Tianmu-1 (TM-1) GNSS-R constellations for Earth surface observation [17], [18], [19], [20]. The ESA Passive REflecTomeTry and dosimetrY (PRETTY) satellite (for GNSS-R altimetry) was launched in October 2023 [21], and

Manuscript received 27 April 2024; revised 3 June 2024; accepted 14 June 2024. Date of publication 18 June 2024; date of current version 24 July 2024. This work was supported in part by the Yunnan Fundamental Research Projects under Grant 202401CF070151, in part by the National Natural Science Foundation of China under Grant 42161067, in part by the Major Scientific and Technological Projects of Yunnan Province: Research on Key Technologies of Ecological Environment Monitoring and Intelligent Management of Natural Resources in Yunnan under Grant 202202AD080010, and in part by the Innovative Training Plan Program for College Students of Yunnan Province under Grant S202310674221. *(Corresponding author: Jinwei Bu.)*

The authors are with the Faculty of Land Resources Engineering, Kunming University of Science and Technology, Kunming 650093, China (e-mail: b_jinwei@kust.edu.cn; 202210108133@stu.kust.edu.cn; 202210102105@stu.kust.edu.cn; 202210102116@stu.kust.edu.cn; liuxinyu6@stu.kust.edu.cn; zxq@kust.edu.cn).

Digital Object Identifier 10.1109/JSTARS.2024.3415754

the NASA Signals of Opportunity P-band Investigation mission (first reflectometry mission at P-band) is expected to be launched in 2024. The hydrological global navigation satellite system (HydroGNSS) is planned to be launched in 2025 by ESA and targets to collect data on the hydrological climate variables [22].

GNSS-R technology applications in the field of Earth observation are rapidly growing. Jin et al. [23], [24] reviewed the potential of GNSS refraction, reflection, and scattering signals in RS of the atmosphere, oceans, land, hydrology, and cryosphere, and pointed out that they play a key role in the prediction of strong winds, hazardous sea states, flood risk, ocean eddies, and storm surges. Camps et al. [25] summarized the main techniques for land monitoring using opportunity signals from GNSS [both reflection (GNSS-R) and transmission (GNSS-T)], which can be used to measure parameters such as SM, surface topography and water level, vegetation, and snow height. They have the advantages of low cost, strong anti-interference ability, and high spatial resolution. GNSS RS techniques also show great potential for atmospheric sensing and detection of geophysical parameters. Yu et al. [26] stated that GNSS radio occultation can be used to measure parameters such as water vapor, temperature, pressure, and humidity in the atmosphere, while GNSS-R can be used to monitor geophysical parameters such as sea surface wind speed, sea surface height, SM, biomass, snow/ice depth, and so on. Wu et al. [27], [28] highlighted that GNSS-R has a potential for SM monitoring and vegetation monitoring, respectively, but currently faces some challenges. In SM monitoring, issues such as coherent and incoherent component extraction, multiangle observation, vegetation, and roughness influence removal, as well as equivalent isotropic radiated power (EIRP) calibration and radio frequency interference (RFI) suppression, need to be addressed to improve retrieval accuracy and data quality. In terms of vegetation monitoring, it is still in the exploratory research stage, with a focus on qualitative analysis and analysis based on satellite observation data. Future research directions include mining observation geometry and polarization information to determine the optimal observation combination and develop quantitative retrieval methods. Making full use of the scattering properties at different angles and polarizations is the key challenge, but research in these directions will offer more promise and potential for improving vegetation retrieval. Carreno-Luengo et al. [29] provided an overview of the applications of GNSS-R in different areas such as marine, terrestrial, and cryosphere. Pierdicca et al. [30] focused on the application of GNSS-R to land, with special attention to SM, biomass, and soil freeze-thaw monitoring. By analyzing GNSS-R data collected by experimental satellites, the study identified retrieval algorithms for SM and biomass and proposed three objectives for further research: confirmation of simulator prediction capabilities, understanding of signal fluctuation behavior, and extended use of neural network-based retrieval techniques. Future enhancements to datasets and tasks will help improve the accuracy and quality of biogeophysical parameters retrieval. Rodriguez-Alvarez et al. [31], on the other hand, gave an overview of the wide range of applications of GNSS-R in several application areas, such as marine, terrestrial, and cryosphere. However, the review focuses only on selected applications in different areas and is not a comprehensive overview document. Recently, a comprehensive review study by Yang et al. [32] shows that spaceborne GNSS-R SM retrieval needs to address the influence of nontarget parameters, introduce transfer learning and spatial feature fusion, and promote downscaling. Future development should focus on improving the retrieval accuracy and generalization capability for practical applications in areas such as environmental resource monitoring and agricultural production.

In summary, there is a great potential for the application of spaceborne GNSS-R technology in the field of land RS. It can measure important parameters, such as SM, surface topography and water level, vegetation, and soil freeze-thaw status, and has the advantages of low cost, high interference immunity, and high spatial resolution. However, there are still some challenges, such as the influence of nontarget parameters, retrieval accuracy improvement, data quality improvement, and modeling algorithm improvement. Although there have been several review articles covering some of the application areas, there is a lack of a comprehensive review document covering research results in the various application areas and problem areas. A comprehensive review document will help provide a comprehensive perspective and an in-depth analysis, promoting further research and promotion of applications in this field. Therefore, one of the main contributions of this review is to focus on reviewing the applications of spaceborne GNSS-R technology in various aspects of land RS and potential innovative applications in the future, including but not limited to SM, vegetation, and flood monitoring, etc. The second contribution is the first comprehensive review of the China's first Tianmu-1 (TM-1) GNSS-R constellation that is compatible with the four major navigation satellite systems of BeiDou, GPS, GLONASS, and Galileo. The review outlines the overview, advantages, and future application prospects of the Tianmu-1 GNSS-R constellation in various fields. This review article will provide valuable insights into the various applications of spaceborne GNSS-R technology in monitoring and studying land surfaces.

The rest of the article is organized as follows. Section II describes the status of spaceborne GNSS-R constellation development and land application areas. Section III focuses on the application of spaceborne GNSS-R technology in SM monitoring, exploring its importance in agriculture, water resource management, and environmental protection. At the same time, the methodology and significance of soil salinity monitoring will be explored, as well as the potential application of spaceborne GNSS-R technology in this field. Sections IV and V will also cover research progress and future directions in areas such as vegetation monitoring and soil freeze-thaw monitoring. In Section VI, on flood detection, the role of spaceborne GNSS-R technology in flood monitoring and early warning systems will be presented and its potential for reducing damage from natural disasters will be explored. Sections VII–IX will also discuss the application of spaceborne GNSS-R technology to inland water monitoring, wetland dynamics, forest fire disturbance monitoring, and land topography change. Section X gives some future applications. Finally, Section XI provides a discussion and summary of the article.

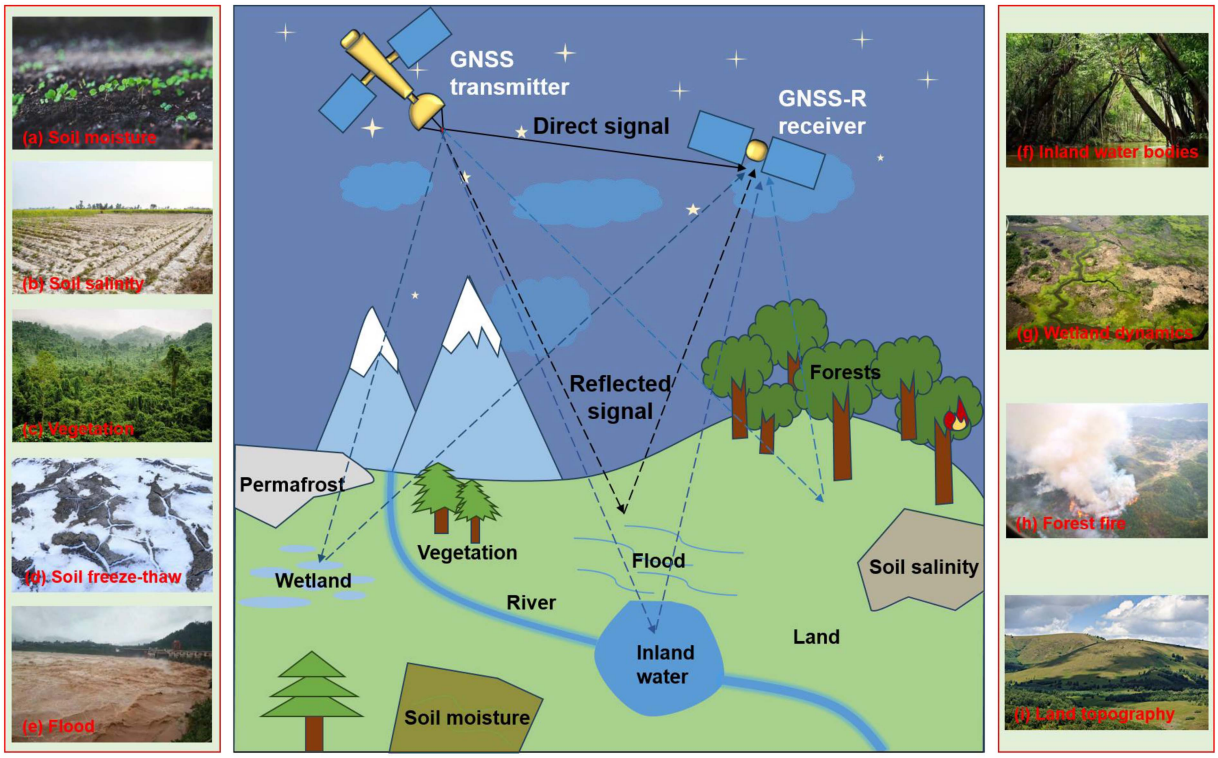

Fig. 1. Typical applications of spaceborne GNSS-R land surface RS. (a) SM, (b) soil salinity, (c) vegetation, (d) soil freeze-thaw, (e) flood detection, (f) inland water bodies, (g) wetland dynamics, (h) forest fire disturbance, and (i) land topographic measurement.

II. Current Development Status and Land Application Fields of Spaceborne GNSS-R Constellations

Over the past two decades, spaceborne GNSS-R technology has made significant breakthroughs in various fields, such as SM, soil salinity, vegetation monitoring, soil freeze-thaw, flood detection, inland water bodies, wetland dynamics, forest fire disturbance, and land terrain measurement, etc.

Fig. 1 shows typical application examples of past and current spaceborne GNSS-R land surface RS. Table I presents the current development status of spaceborne GNSS-R constellations and the application directions in the terrestrial field. The spaceborne GNSS-R technology has breakthrough value in these areas. The application of this technology provides important data support in the fields of environmental monitoring, resource management, and disaster early warning, and is of great significance in promoting sustainable development and ecological protection. Of course, the terrestrial applications of spaceborne GNSS-R technology are not limited to this, and future research should further explore in depth the potential of this technology in different areas.

In addition to the GNSS-R mission mentioned above, there are also other spaceborne missions that use reflected GNSS signals and other opportunity signals for different geophysical applications. For example, on July 5, 2019, DOT-1 satellite was launched, which is the third satellite designed by Surrey Satellite Technology Limited and used for GNSS-R research. The payloads carried on the DoT-1 satellites are designed to test advanced electronic equipment, such as antenna technology, which could be used in future spaceborne technologies [39]. On 3 July 2021, the first commercial satellite with a GNSS-R payload (Jilin-01B) was launched, with the GNSS-R payload on board the Jilin-01B satellite developed by Changguang Satellite Technology, Co., Ltd., to detect a range of ocean parameters [40].

Since July 2021, China's launch of the FY-3E satellite has been followed by the launch of the FY-3F/3G satellite and the TM-1 GNSS-R constellation [41]. Among them, the TM-1 meteorological satellite was developed and operated by China Aerospace Science and Industry Corporation Limited (CASIC), in a sun-synchronous orbit at an altitude of 520 km. As of March 2024, China has successfully launched 23 TM-1 satellites and their operation is stable [the launch status of China's TM-1 constellation satellites is given in Table II (Information is sourced from Aerospace Tianmu (Chongqing) Satellite Science and Technology Co., Ltd. and Aerospace Science and Industry (Beijing) Spatial Information Application Co., Ltd.)] . The latest four satellites, launched on 5 January 2024, have been put into operational use, forming a sun-synchronous orbit operational subconstellation with other satellites in orbit.

This satellite constellation is the first and only commercial satellite in China that meets the operational needs of numerical forecasting in terms of accuracy and timeliness. We plan to construct an occultation meteorological exploration constellation consisting of a sun-synchronous orbit and a low inclination orbit, focusing on the demand for high-quality atmospheric and oceanic RS data from global numerical weather forecasts, catastrophic weather forecasts, and space weather forecasts.

TABLE I
DEVELOPMENT STATUS AND LAND APPLICATION FIELDS OF SPACEBORNE GNSS-R CONSTELLATIONS

Missions	Launch country (Area)	Satellite launch time	GNSS system	Application directions in the land field
UK-DMC [33]	Britain	2003-12	GPS	–
UK-TDS-1 [4, 5]	Britain	2014-07	GPS	SM, vegetation, flood, wetland, soil freezing and thawing, inland water
CYGNSS [6] [7, 8]	America	2016-12	GPS	Soil salinity, SM, vegetation, flood, wetland, soil freezing and thawing, inland water, fire disturbance, land topographic, inland (lake) water body surface height, river slope, river width, lake ice, reservoir water level, etc.
^{3}Cat-2 [9]	Spain	2016-08	GPS GLONASS Galileo BeiDou	–
SMAP GNSS-R [34]	America	2015-01	GPS	SM, vegetation, soil freezing and thawing state
BF-1 A/B [14], [15], [16]	China	2019-06	GPS BeiDou	SM
Spire [11], [12], [13]	America	2019-01	GPS Galileo BeiDou Quasi-Zenith Satellite System (QZSS)	SM, inland (lake) water body surface height
FY-3E/3G/3F [17], [18], [19], [20]	China	2021-07/2023-04/2023-08	GPS Galileo BeiDou	soil freezing and thawing, SM (FY-3E)
^{3}Cat-5 A/B (FSSCat) [10]	Spain	2020-09	GPS Galileo	SM
^{3}Cat-4 [35, 36]	Spain	Summer 2024 (expected)	GPS Galileo	–
PRETTY [21]	ESA	2022	GPS Galileo	–
TRITON (FORMOSAT-7R) [37, 38]	Taiwan, China	2022	GPS Galileo QZSS	–
HydroGNSS [22]	ESA	In the future	GPS Galileo	SM, biomass, flood, wetland, soil freezing and thawing state

This will form a global all-weather, all-time, and integrated three-dimensional operational detection capability for the ocean, atmosphere, and ionosphere, with global coverage and increased density in mid and low latitudes. Compared with BF-1 A/B and FY-3E/3G, TM-1 has four significant advantages.

1) Complementary with FY, the data processing algorithms are consistent with FY satellites, and the constellation configuration is complementary and collaborative with FY satellites.
2) Four-system compatibility, it is China's first detection constellation that is compatible with the four navigation satellite systems of Beidou, GPS, GLONASS, and Galileo.
3) Integrated detection, which can simultaneously achieve integrated three-dimensional detection of GNSS occultation and GNSS-R, is the first commercial constellation in the world to achieve multicircle and multielement detection of "sea antiatmospheric occultation ionization occultation." It can obtain real-time information on sea surface wind field, sea ice, SM, as well as environmental factors, such as atmospheric temperature, humidity, pressure, and ionospheric electron density profiles. In addition, it is expected that in the near future, TM-1 GNSS-R (including BeiDou-R, GPS-R, GLONASS-R, and Galileo-R) data can be used for wind speed retrieval, typhoon monitoring, real-time monitoring of shipping routes, dynamic regulation of marine fisheries, and ecological RS monitoring (such as soil moisture, water identification, flood monitoring, water eutrophication monitoring (such as blue-green algae)), among other areas.
4) High spatiotemporal resolution, which can achieve a three-dimensional atmospheric and oceanic detection capability that covers the global sea surface in 3 h, with a grid spacing of 6 h and 200 km.

TABLE II
LAUNCH STATUS OF CHINA'S TM-1 CONSTELLATION SATELLITES

Satellite number	R&D institutions	Date of launch
Tianmu-1 00	CASIC	14 October 2021
Tianmu-1 01	CASIC	9 January 2023
Tianmu-1 02	CASIC	9 January 2023
Tianmu-1 03	CASIC	22 March 2023
Tianmu-1 04	CASIC	22 March 2023
Tianmu-1 05	CASIC	22 March 2023
Tianmu-1 06	CASIC	22 March 2023
Tianmu-1 07	CASIC	20 July 2023
Tianmu-1 08	CASIC	20 July 2023
Tianmu-1 09	CASIC	20 July 2023
Tianmu-1 10	CASIC	20 July 2023
Tianmu-1 11	CASIC	25 December 2023
Tianmu-1 12	CASIC	25 December 2023
Tianmu-1 13	CASIC	25 December 2023
Tianmu-1 14	CASIC	25 December 2023
Tianmu-1 15	CASIC	5 January 2024
Tianmu-1 16	CASIC	5 January 2024
Tianmu-1 17	CASIC	5 January 2024
Tianmu-1 18	CASIC	5 January 2024
Tianmu-1 19	CASIC	27 December 2023
Tianmu-1 20	CASIC	27 December 2023
Tianmu-1 21	CASIC	27 December 2023
Tianmu-1 22	CASIC	27 December 2023

Currently, there is no literature reporting on related work based on TM-1 data, one of the main reasons being that the data are not publicly available for free. However, the data can be used for free among participating members and some research institutions after being approved and authorized by Aerospace Tianmu (Chongqing) Satellite Science and Technology Co., Ltd. and Aerospace Science and Industry (Beijing) Spatial Information Application Co., Ltd. The authors of the article have also been approved and authorized by this company to use TM-1 data, which includes three levels: L0, L1, and L2. Among them, L0 level includes the raw intermediate frequency signals of GPS, BeiDou, Galileo, and GLONASS. L1 level includes delay Doppler maps (DDMs), GNSS reflection event occurrence time and location, reflected GNSS satellite number, reflected GNSS satellite position and velocity, the position and velocity of the TM-1 satellite, the normalized bistatic radar scattering cross-section (NBRCS) at specular points (SPs), and leading edge slope (LES). L2 level includes the sea surface wind speed products and land surface SM products obtained from the reflection signals of GPS, BeiDou, Galileo, and GLONASS.

Fig. 2 shows the satellite trajectory and SP trajectory of the TM-102 subsatellite in 24 h. As shown in the figure, the TM-102 subsatellite can observe the Earth's surface in the latitude range of 90° N and 90° S with high spatial and temporal resolution. Therefore, it has a wider coverage range than the CYGNSS satellite, which will expand the innovative application of spaceborne GNSS-R technology in polar regions.

Fig. 3 shows the four DDM raw counts of BeiDou, GPS, Galileo, and GLONASS over the (a)–(d) ocean, (i) and (j) land, and (k) and (l) sea ice on June 29, 2023, along with their delay waveforms (DWs) with a Doppler of 0 Hz. As shown in the figure, the DDM raw counts delay and Doppler range of the TM-1 constellation satellite are different from that of FY-3E, CYGNSS, BF-1, and TDS-1, with a delay and Doppler size of 61 × 20 (i.e., 61 × 20 array of DDM bin raw counts). Under incoherent scattering, all DDMs exhibit a similar "horseshoe shape." The second peak can be observed in the delay dimension of Galileo DDM, which is related to the relevant characteristics of BOC modulation. Under coherent scattering, the signal-to-noise ratio (SNR) is very high, and the power values of each DDM are concentrated near the SP. The Galileo DDM presents a unique shape of triple peaks due to its BOC modulation.

Fig. 4 shows an example of the effective scattering area of BeiDou, GPS, Galileo, and GLONASS signals collected by TM-1. As can be seen from the figure, the delay and Doppler range of the TM-1 constellation satellite are consistent with that of FY-3E, with a delay and Doppler size of 20 × 9, that is, the delay range is [-0.875:0.125:1.5] chips, and the Doppler frequency range is [-1000:250:1000] Hz. Figs. 3 and 4, respectively, show the DDM bin raw counts and integral DW extracted from DDM bin raw counts of BeiDou, GPS, Galileo, and GLONASS signals collected by TM-1.

The authors of the article are currently conducting research on spaceborne GNSS-R based on TM-1 data, and the research results of related applications based on this data will be reported in subsequent articles. At present, the TM-1 constellation data have been pushed in real time to the China Meteorological Administration, completing the business access of the China Meteorological Administration's meteorological data products, and applied in the numerical weather forecast business system. Subsequently, Aerospace Systems Corporation will also deploy low inclination subconstellations to strengthen key area exploration and form a comprehensive three-dimensional detection capability for global coverage, mid-low latitude encrypted atmosphere, and ocean.

III. RETRIEVING SOIL MOISTURE AND SOIL SALINITY USING SPACEBORNE GNSS-R

A. Soil Moisture Retrieval

SM is an important factor in researching the interaction of water, energy, and biogeochemical fluxes between the Earth's near-surface land and the atmosphere. Currently, the main specialized satellites used to obtain SM information are: SM active passive (SMAP), SM and ocean salinity (SMOS), CYGNSS, and so on. Early satellites used for SM retrieval were: the METEOrological Operational Satellite (METOP) and the European RS Satellite (ERS-1 and ERS-2).

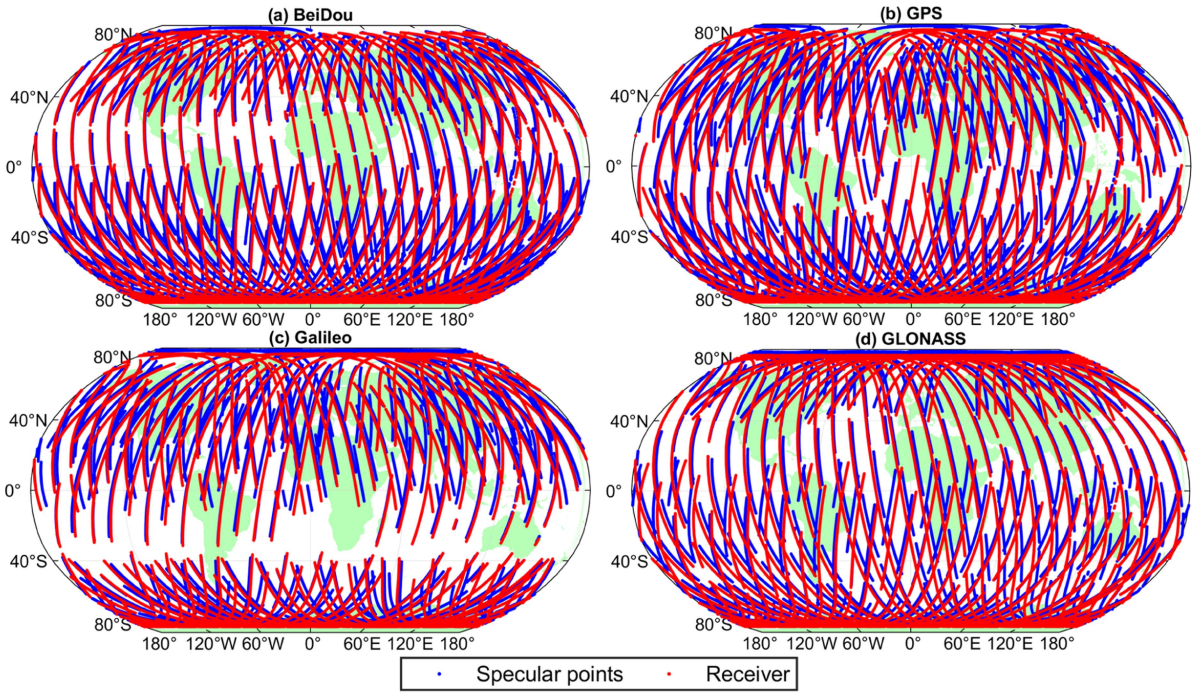

Fig. 2. SPs and receiver subsatellite (TM-1 02) points; the observation date is 29 June 2023.

SM retrieval can be measured using L-band microwave radiation, Radar, or SAR. Although the spatial resolution of the L-band microwave radiometer on the satellite is poor (around tens of kilometers), the radar system is more affected by surface roughness effects. Rodriguez-Alvarez et al. [42] proposed a new technique for retrieving SM using GNSS signals reflected on the soil surface. This technique exploited the power fluctuations of the signal generated by the interference between the direct GPS signal and the reflected signal from the soil surface. Camps et al. [43] used the GNSS-R data of TDS-1 to study the sensitivity of SM and normalized difference vegetation index (NDVI) of different surface types, and the results showed that the GNSS-R reflected signal was more sensitive to SM when the NDVI was low, and the sensitivity decreased but was still significant with the increase of NDVI. Chew et al. [44] used TDS-1 data to study the ability of the bistatic radar system to sense SM changes and found that the sensitivity of the reflected signal to SM change was 7 dB and discussed that the spatial resolution of the spaceborne GNSS-R SM retrieval can be improved by quantifying the influence of ground roughness degree and vegetation on the reflected signal. However, since the TDS-1 sensor only operates for two days in an eight-day cycle, its data acquisition is severely limited in terms of spatial and temporal coverage, making it impossible to estimate daily SM. Kim and Lakshmi [45] investigated the limitations and capabilities of CYGNSS observations for SM estimation and introduced relative signal-to-noise ratio (SNR) values from CYGNSS DDMs to improve the temporal resolution of SMs derived from SMAP data. Chew and Small [46] compared the CYGNSS observations with the SMAP SM retrieval and with the in situ SM observations, and the results showed a consistent linear relationship between the CYGNSS observations and the SMAP retrieval.

At present, several new spaceborne GNSS-R missions have also demonstrated the potential for SM retrieval. BF-1 satellite is a pilot mission for the GNSS-R constellation in China. Wan et al. [16] preliminarily demonstrated that this mission can provide a new spaceborne GNSS-R data source for SM estimation using a three-month sample of BF-1 A/B. FY-3E is the fifth satellite in China's series of polar-orbiting meteorological satellites. Yang et al. [47] proposed an effective SM retrieval method for the FY-3E GNSS occultation sounder II-reflectometer (GNOS-R). However, GNSS-R research has focused on GPS consisting only of medium-Earth orbit satellites, while the use of geostationary orbit (GEO) satellites (such as those in the BeiDou Navigation Satellite System) has received little attention. Ban et al. [48] proposed two methods for estimating SM using GEO signals, namely GEO Interferometric Reflectometer (GEO-IR) and GEO Reflectometer (GEO-R), and the results showed that the proposed GEO-IR and GEO-R can reliably monitor SM under bare soil conditions, enhancing GNSS-R by significantly reducing treatment complexity and increasing time coverage. Due to the uncertainty of the physical characteristics of the site, the complexity of the retrieval process, and the nonlinearity of the GNSS-R SM retrieval, there are still some challenges in the accurate retrieval of SM. Machine learning (ML) methods are flexible and able to handle nonlinear problems. Eroglu et al. [49] proposed a physically aware ML method by obtaining the nonlinear dependence of CYGNSS observables with SM values and geophysical parameters representing vegetation and ground effects. Jia et al. [50] tested and analyzed the SM retrieval performance of the dual base GNSS-R using ML-assisted methods. In addition, Jia et al. [51] also proposed using two typical ML methods, random forest (RF) and support vector machine (SVM), to perform SM retrieval from GNSS-R data from self-designed

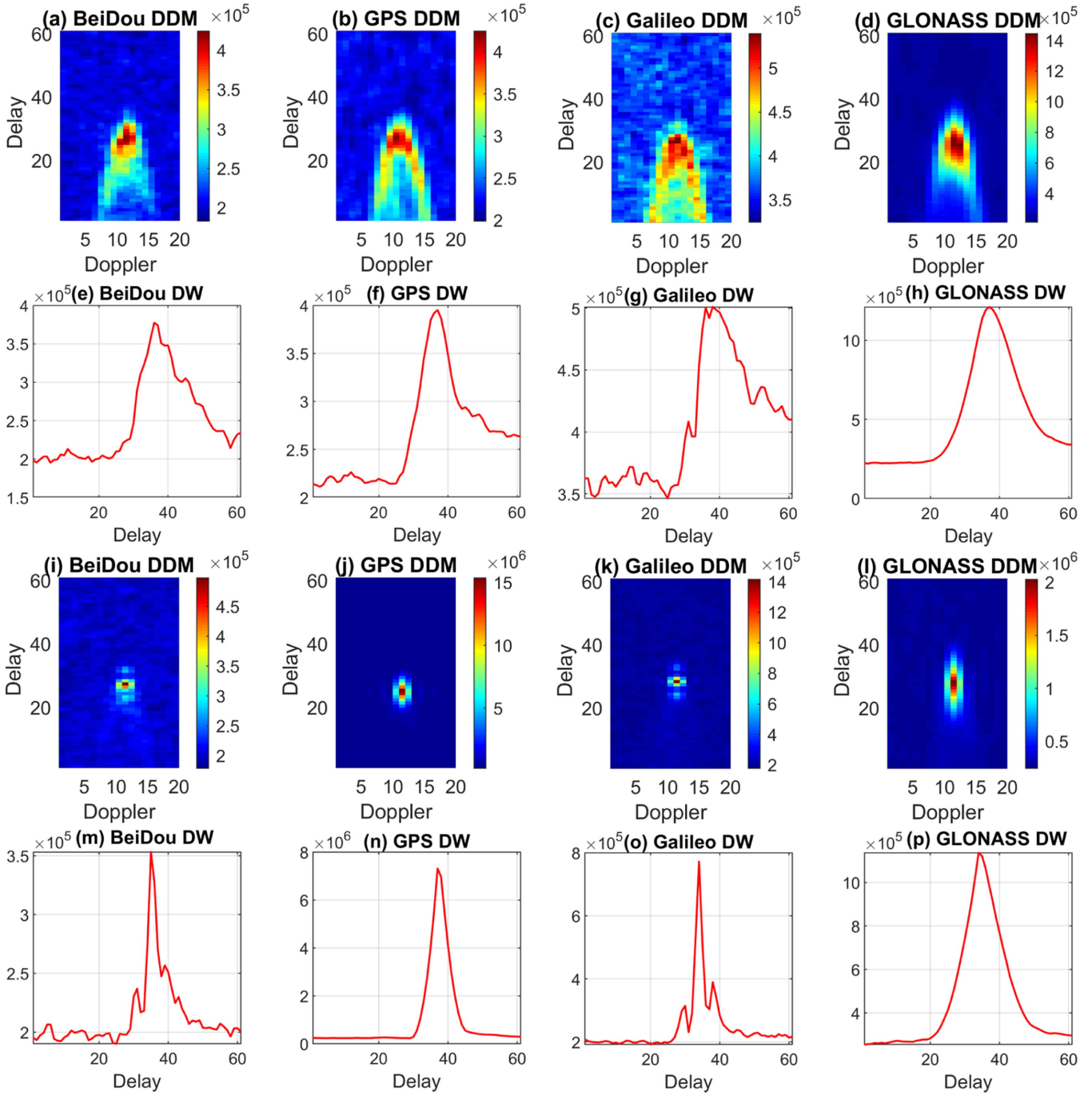

Fig. 3. DDMs and corresponding DWs in raw counts from BeiDou, GPS, Galileo, and GLONASS, respectively, over (a)–(h) ocean and (i), (j), (m), (n) land, and (k), (l), (o), (p) sea ice. Data were collected on 29 June 2023. The SNRs of (a), (b), (c), and (d) are 0.50 dB, -0.29 dB, -4.01 dB, and 7.22 dB, respectively. The incidence angles of (a), (b), (c), and (d) are 10.18°, 15.91°, 22.23°, and 28.40°, respectively. The SNRs of (i), (j), (k), and (l) are 1.85 dB, 18.05 dB, 7.86 dB, and 8.25 dB, respectively. The incidence angles of (i), (j), (k), and (l) are 20.57°, 16.52°, 46.86°, and 38.83°, respectively.

experiments (in-situ and airborne). Yan et al. [52] established an effective schematic for SM estimation based on CYGNSS data, and the use of CYGNSS SM significantly improved the pantropical coverage of SMAP, with an average increase of about 22%. Senyurek et al. [53] proposed an ML-based framework for estimating SM using CYGNSS observations of International Soil Moisture Network (ISMN) sites in the Continental United States (CONUS). Santi et al. [54] developed an algorithm based on artificial neural networks (ANNs) for retrieving SM and forest aboveground biomass (AGB) from GNSS-R observations. The CYGNSS generates DDMs containing important Earth surface information through GNSS reflection measurements. Because the peak value of DDM is not only affected by SM but also by complex topography, inundation, and overlying conditions, there is significant uncertainty. The application of deep learning (DL)-based techniques may extract additional information from

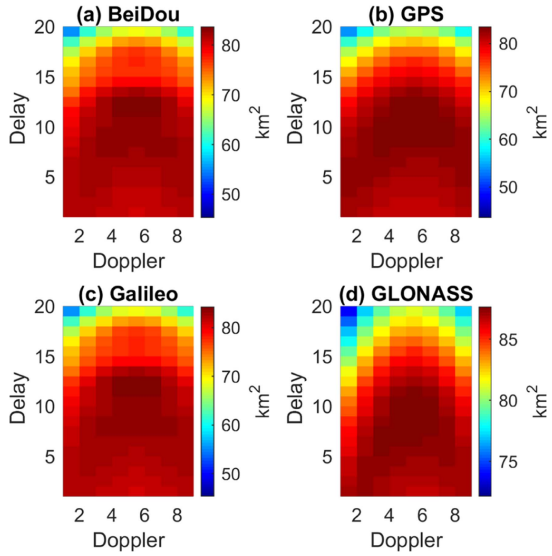

Fig. 4. Effective scattering area of (a) BeiDou, (b) GPS, (c) Galileo, and (d) GLONASS signals collected by TM-1.

the entire DDM, which has advantages over existing ML-based analyses. Roberts et al. [55] investigated the data-driven approach of convolutional neural networks (CNNs) to determine the complex relationship between reflection measurements and surface parameters, providing a basis for achieving improved mechanisms for global SM estimation. Nabi et al. [56] conducted a comprehensive evaluation of DL models and publicly available CYGNSS-based SM products at a quasi-global scale. Hu et al. [57] used massive monitoring data from multiple GNSS observation stations, combined with GNSS-R technology and DL algorithms, to study the SM retrieval method for river slope in the study area. However, the global SM retrieved by GNSS-R is significantly affected by the presence of water bodies. Yang et al. [58] proposed a water removal method for global spaceborne GNSS-R SM retrieval, which can maximize the retention of water surface area and effectively remove the impact of water on SM. Wang et al. [59] addressed the significant impact of water on the surface reflectance (SR) of CYGNSS and improved the removal method of water influence based on the spatial resolution of CYGNSS data. In the future, the GNSS-R SM retrieval model of DL can be optimized to obtain more realistic and reliable SM, and this retrieval model can be used to solve practical application problems.

To sum up, SM is estimated based on the sensitivity of GNSS-R reflectivity to SM, but noise in the observations can significantly affect the SM estimation results. For this reason, the existing literature has done a lot of research work to address the above-mentioned problem and considered the effects of roughness and vegetation on the effective GNSS-R reflectivity. Assuming that the reflected signal on land is mainly determined by coherent reflection, the reflectivity under coherent reflection can be calculated as follows [60]:

$$\Gamma(\theta) = \frac{(4\pi)^2 (P_r - N)(R_r + R_t)^2}{\lambda^2 P_t G_t G_r} \tag{1}$$

where θ is the angle of incidence; P_r is the peak power of the DDM; $N$is the background noise; R_t and R_r are the distances from the transmitter and receiver to the specular reflection point, respectively; $P_t G_t$ is the transmitter EIRP; G_r is the reflective antenna gain; λ is the GNSS signal wavelength.

Reflectance is related to several physical properties of the surface. First, SM has a major influence on the reflectance of sparsely vegetated (<5 kg/m^2) and flat terrain due to the surface soil dielectric constant. Second, vegetation attenuation plays an important role in densely vegetated areas (e.g., tropical forests). Third, surface roughness also has an effect on reflectance due to diffuse scattering. It is worth noting that for spaceborne observations, the effect of topography is greater than that of small-scale roughness [61]. Therefore, it is important to correct reflectance for vegetation attenuation and terrain roughness attenuation.

As the GNSS reflection signal is absorbed by the vegetation canopy, the observed reflectance can be corrected to that of the soil surface

$$\Gamma_{\text{soil}}(\theta) = \Gamma(\theta)/\gamma \tag{2}$$

where $\Gamma(\theta)$ is the observed reflectance calculated from (1); $\Gamma_{\text{soil}}(\theta)$ is the reflectance at the soil surface; θ is the angle of incidence; γ is the two-way attenuation of biomass canopy derived as

$$\gamma = \exp(-2 \cdot b \cdot \text{vwc}/\cos(\theta)) \tag{3}$$

where vwc is the vegetation moisture content obtained from the SMAP data product; b is a constant parameter depending on signal wavelength, polarization, and vegetation classification. For a wavelength of about 20 cm, the parameter b ranges from 0.09 to 0.15 for different land cover classifications [62]. The International Geosphere-Biosphere Programme (IGBP) lookup table is usually used for IGBP classification and a value of b is set for each IGBP category according to the SMAP algorithm theoretical basis documents.

For spaceborne GNSS-R observations, the effect of large-scale roughness on DDM observations is even greater. The terrain roughness attenuation effect can be expressed as follows:

$$Att_{\text{roughness}} = \Gamma_{\text{soil}}/\Gamma_{\text{fresnel}}. \tag{4}$$

The reflectivity of the soil surface Γsoil could be calculated with (1) and (2), and the Fresnel reflectivity Γ_{fresnel} is dependent on the surface soil dielectric constant ε and the incidence angle θ, defined as follows:

$$\Gamma_{\text{fresnel}} = |R_{rl}(\theta)|^2 = \frac{(\varepsilon - 1)^2 \cos^2\theta \left(\varepsilon - \sin^2\theta\right)}{\left(\varepsilon \cos\theta + \sqrt{\varepsilon - \sin^2\theta}\right)^2 \left(\cos\theta + \sqrt{\varepsilon - \sin^2\theta}\right)^2} \tag{5}$$

where R_{rl} denotes the Fresnel reflection coefficient. For GNSS-R measurements, the transmitted signal is in right-hand circular polarization, and the reflected signal is in left-hand circular polarization (LHCP).

Typically, SM retrieval using spaceborne GNSS-R makes the algorithmic assumption that, given a particular location, the only

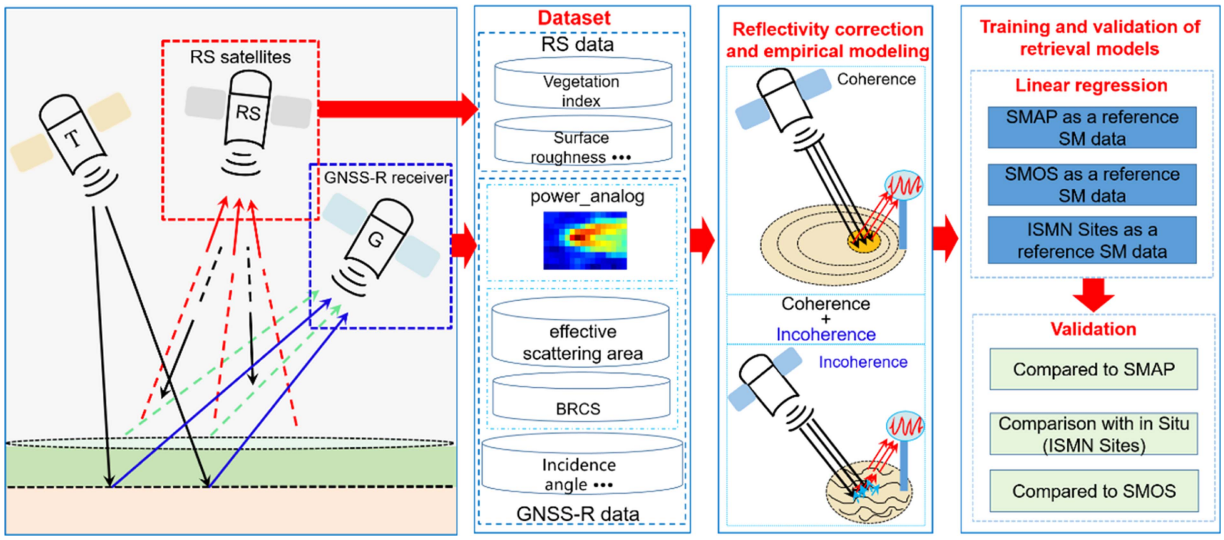

Fig. 5. Schematic diagram of the spaceborne GNSS-R SM retrieval process.

variables that change over time are SM and biomass, while soil surface roughness (topography) and soil texture remain constant. In this case, GNSS-R reflectivity may be linearly related to the reference SM (e.g., SMAP data) for each terrain grid cell

$$\mathrm{sm} = a \cdot \Gamma_{\mathrm{soil}} + b \tag{6}$$

where sm denotes the soil moisture reference data; the parameters a and b are polynomial fit coefficients, Γ_{soil} represents the observed reflectivity with vegetation correction, which could be derived from (1) to (3).

Currently, the primary approach involves utilizing surface roughness and vegetation index RS data as auxiliary factors to mitigate the influence. Once the reflectivity is obtained, it can construct an SM retrieval model using empirical models or ML methods based on surface reflectivity. The schematic diagram of the spaceborne GNSS-R SM retrieval process is shown in Fig. 5.

ML is a powerful data-driven approach for environmental monitoring of rapidly growing RS data. Compared with traditional physical and empirical models, ML methods have better scalability. According to the complexity of the model, ML methods can be divided into two categories: traditional ML methods and DL methods. Traditional ML methods include linear models, shallow neural networks (NNs), SVMs, decision tree-based learning methods, and ensemble learning methods. These methods are suitable for situations with limited sample datasets. However, they may have difficulty in capturing the periodicity and continuity of time series data. DL models are neural network (NN) models with complex network structures, typically composed of multiple layers. The GNSS-R SM retrieval method is the process of solving regression problems, and traditional regression equation fitting may have errors. ML methods can continuously approximate real relationships, typically including data preprocessing, feature extraction, dataset splitting, model training, and model testing. The schematic diagram of constructing a GNSS-R SM retrieval model using ML method is shown in Fig. 6.

As given in Table III, the summary and comparison are mainly from several aspects, including observation satellites, GNSS-R observations, main components of the reflected signal, spatial coverage, spatial resolution, reference data, auxiliary data, validation data, retrieval models, and specific details of the main results.

B. Soil Salinity Retrieval

In recent years, the problem of soil salinization, which has degraded the destruction of soil structure and the reduction of microbial populations, has become increasingly prominent, seriously affecting global food security. Furthermore, soil salinization will have serious impacts on global infrastructure security and geological hazards in the coastal zone. Currently, soil salinization is predominantly found in arid and coastal areas; soil salinity monitoring is of great significance for agricultural production management, soil improvement and restoration, environmental protection, and ecological restoration, as well as land planning and decision support.

The rapid development of GNSS-R technology provides a new approach for large-scale soil salinity retrieval. This technique is based on the interaction between the microwave signals emitted by GNSS satellites and the signals reflected back from the ground surface, and by analyzing the characteristic parameters of the reflected signals, such as phase, amplitude, and polarization, information such as soil salinity and water content can be deduced, thus realizing the monitoring and assessment of soil salinization [73]. The CYGNSS is a satellite mission of NASA of the United States of America designed to monitor and predict hurricanes and storm surges using an observing system of small satellites. The CYGNSS satellite crew consists of eight microsatellites, each carrying four reflectometry channels to receive GPS L1-C/A coded scattering signals from the Earth's surface. These satellites orbit the Earth near the equator and acquire data from the ocean surface by reflecting microwave

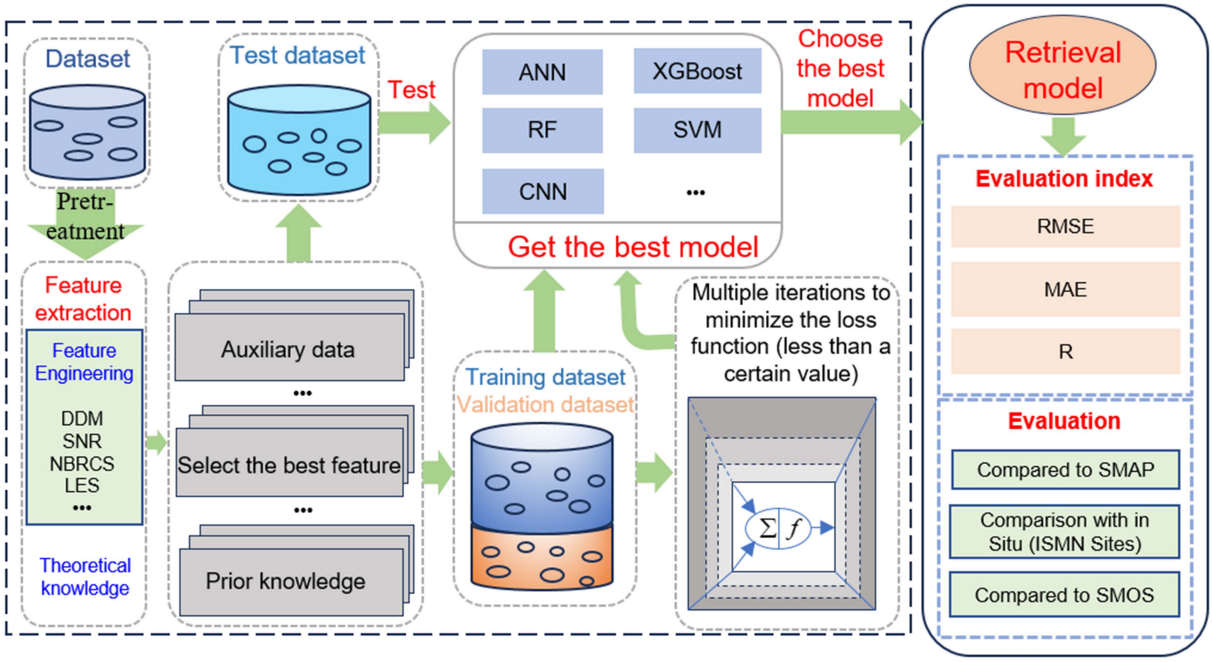

Fig. 6. Schematic diagram of constructing an GNSS-R SM retrieval model using ML method.

signals. These data can be used to generate high-resolution information on the path and intensity of storm surges and hurricanes, contributing to improved early warning and response to natural disasters. The minimum spatial footprint of CYGNSS is about 3 × 0.5 km when the scattered signal is dominated by the coherent part, and it is larger when the surface around the signal reflection point is rougher [74]. The temporal resolution of CYGNSS is quite high with an average revisit time of 7.2 h [75]. Currently, CYGNSS has demonstrated a powerful measurement capability not only for ocean surface geophysical parameters, such as ocean surface wind speed [8], ocean altimetry [76], tropical hurricane energy estimation [77], and sea surface salinity [78], but also for a wide range of land-based RS applications, such as soil humidity [52], soil freezing and thawing [107], and flood inundation [79]. CYGNSS is an attractive method for large-scale soil salinity measurements because the L-band of GNSS signals collected by CYGNSS is well suited for soil condition monitoring [46]. Compared with optical satellite RS satellites, CYGNSS can provide high temporal resolution surface observations in real-time. Strong correlations between GNSS-R signal reflectivity and soil salinity have been found for specific polarization and angle combinations, demonstrating the feasibility of using GNSS-R signals to retrieve soil salinity [73], [80]. In 2023, Wang et al. [80] demonstrated the possibility of using CYGNSS data to retrieve soil salinity based on a soil dielectric model by constructing a soil salinity retrieval model using the imaginary part of the improved Dobson-S model as a basis. However, it remains a challenge to quantify the complex nonlinear relationship between Fresnel reflectance and soil salinity. For this reason, Wang et al. [81] proposed a CYGNSS-based model for soil electrical conductivity retrieval (CIG), which is different from previous studies in that it is corrected for surface characteristics, such as vegetation attenuation and surface roughness. The use of geometrical-optical models instead of the two-base radar equations is more applicable to CYGNSS. In addition, the mean square slope parameters were introduced to effectively describe the surface roughness. The gradient boost regression tree algorithm was used to combine Fresnel reflectance and auxiliary variables to make the model more adaptable to complex nonlinear relationships. Using CYGNSS data provides better sensitivity to soil salinity compared to traditional ML methods. The results showed a correlation coefficient of 0.730, a root-mean-square error (RMSE) of 1.318 mS/cm, and an average absolute error of 0.570 mS/cm. The proposed soil salinity model based on CYGNSS data can provide a promising method for monitoring land salinity on a large scale. However, the strong spatial heterogeneity of soil salinity and the occurrence of data defects or outliers on the long time series due to the influence of weather, instrumentation, and other reasons lead to certain difficulties in the validation process.

In summary, there is an urgent need to develop the best methodology for monitoring soil salinity using spaceborne GNSS-R data.

IV. Vegetation Monitoring Using Spaceborne GNSS-R

Vegetation is an important part of the Earth's ecosystem, and the vegetation types in each region are influenced by local climate, soil, and other environmental factors. Vegetation plays a crucial role in maintaining biodiversity, soil conservation, water cycling, and climate regulation.

Spaceborne GNSS-R is a popular vegetation monitoring method at present, which can measure key parameters of land vegetation through GNSS reflection signals. With the launch of

TABLE III
RETRIEVAL APPROACH AND ACCURACY OF CURRENTLY PUBLISHED SPACEBORNE GNSS-R SM RETRIEVAL STUDIES[1]

Source	Satellites	GNSS-R Observables	Main Components	Spatial Temporal Coverage	Spatial Resolution	Reference SM data for training models	Auxiliary Data	Validation SM data for testing models	Retrieval Models	Main Results (cm^3/cm^3)
Chew and small [46]	CYGNSS	Reflectivity	Coherent	Quasi-Global	36 km × 36 km	SMAP	LAI	SMAP, in situ	Linear regression	median ubRMSE = 0.045
Kim and Lakshmi [45]	CYGNSS	Reflectivity	Coherent	Regional (CONUS)	9 km × 9 km	SMAP	GPM, VWC, landcover types	SMAP	Linear regression	For different observation conditions: R = 0.67/0.68/0.77
Al-Khaldi et al. [63]	CYGNSS	BRCS	Incoherent	Quasi-Global	25 km × 25 km	SMAP	—	SMAP	Time-Series technique	R = 0.82, RMSE = 0.04
Munoz-Martin et al. [64]	FSSCat	Reflectivity, SNR, incidence angle	Coherent	Regional (above 45°N)	36 km × 36 km	SMOS	FMPL-2 MWR radiometry data	SMOS	ANN	R = 0.79, STD (error) = 0.063
Santi et al. [65]	CYGNSS	Reflectivity, SNR, incidence angle	—	Quasi-Global	—	SMAP	VOD	SMAP	ANN	R = 0.85, RMSE = 0.069
Yan et al. [52]	CYGNSS	Reflectivity (maximum, mean, variance, skewness, kurtosis)	Coherent	Quasi-Global	36 km × 36 km	SMAP	VOD	SMAP	Linear regression	R = 0.80, RMSE = 0.07
Jia et al. [66]	CYGNSS	Reflectivity	Coherent	Quasi-Global	36 km × 36 km	SMAP	VOD, roughness coefficient	SMAP, in situ	XGBoost with preclassification strategy	ubRMSE = 0.052, R = 0.86 (vs SMAP) ubRMSE = 0.049, R = 0.753 (vs in-situ)
Jia et al. [67]	CYGNSS	Reflectivity, TES, dielectric constant, incidence angle	Coherent	Quasi-Global	9 km × 9 km	SMAP	Land type	SMAP	XGBoost with an LT digitization strategy	R = 0.71, RMSE = 0.063
Clarizia et al. [60]	CYGNSS	Reflectivity	Coherent	Quasi-global	36 km × 36 km	SMAP	SMAP	SMAP, SMOS	Trilinear Regression	RMSE = 0.07 (vs SMAP)
Eroglu et al. [49]	CYGNSS	Reflectivity, TES, LES, incidence angle	Both	Sites	9 km × 9 km	ISMN Sites	Elevation, Slope, NDVI, VWC, h-parameter (surface roughness)	ISMN Sites	ANN	RMSE = 0.0544, R = 0.9009 (vs in-situ)
Senyurek et al. [68]	CYGNSS	Reflectivity, TES, incidence angle	Coherent	Sites	9 km × 9 km	ISMN Sites	Elevation, NDVI, VWC, soil clay ratio, and soil silt ratio	ISMN Sites	RF	ubRMSD = 0.044, R = 0.66 (vs SMAP)
Lei et al. [69]	CYGNSS	Reflectivity, TES, incidence angle	Coherent	Quasi-global	9 km × 9 km	SMAP	Elevation data, Global Surface Water Dataset, MODIS NDVI and Land Cover Type	SMAP	RF	ubRMSD = 0.0395, R = 0.4006 (vs SMAP) ubRMSE = 0.0543, R = 0.4623 (vs in-situ)
Zhu et al. [70]	CYGNSS	Reflectivity	Coherent	Quasi-Global	_	SMAP	VOD, SST	SMAP, in situ	Linear regression	R = 0.929, RMSE = 0.043 (vs. SMAP) R = 0.927, RMSE = 0.042 (vs. in situ)
Zhang et al. [71]	CYGNSS	Reflectivity (maximum, mean, variance, skewness,	Coherent	Regional (CONUS)	36 km × 36 km	SMAP	VOD, SST	SMAP, in situ	Linea regression	R = 0.815, RMSE = 0.066 (vs. SMAP) R = 0.549, RMSE = 0.078 (vs. in situ)
Yang et al. [72]	TDS-1, CYGNSS	Reflectivity	Coherent	Regional (China)	36 km × 36 km	SMAP	Elevation, slope, NDVI, VWC, roughness data, precipitation	SMAP, in situ	BP-ANN	R = 0.676/0.798, ubRMSE = 0.060/0.062, MAE = 0.052/0.040 (TDS-1/CYGNSS vs. SMAP) R = 0.687/0.724, ubRMSE = 0.056/0.053, MAE = 0.066/0.052 (TDS-1/CYGNSS vs. in situ)
Wan et al. [16]	BF-1 A/B	Reflectivity	Both	Quasi-Global	36 km × 36 km	SMAP	—	SMAP, in situ	Linear regression	R = 0.94, RMSE = 0.029 (vs. SMAP) R = 0.77, RMSE = 0.049 (vs. in situ)
Yin et al. [62]	FY-3E	Reflectivity (GPS/BDS/GAL)	Coherent	Global	36 km × 36 km	SMAP	VWC, IGBP classification	SMAP, in situ	Linear regression	R = 0.83/0.85/0.86, RMSE = 0.0503/0.0497/0.0482 (GPS/BDS/GAL vs. SMAP) Mean RMSE = 0.054 (GPS/BDS/GAL vs. in situ)
Setti. et al. [13]	Spire	Reflectivity (GPS/mult)	Coherent	Regional (Southeast Australia		SMAP	—	SMAP, in situ	Linear regression	R = 0.85, median ubRMSE = 0.062 (Spire-multi vs. SMAP) median ubRMSE = 0.057 (Spire-multi vs. in situ)

[1]BRCS: bistatic radar scattering cross-section; SNR: signal-to-noise ratio; TES: trailing edge slope; LES: leading edge slope; LAI: leaf area index; GPM: global precipitation measurement; VWC: vegetation water content; NDVI: normalized difference vegetation index; VOD: vegetation optical depth; SST: soil surface temperature; RMSE: root-mean-square error; R: correlation coefficient; ubRMSE: unbiased root-mean-square error; ubRMSD: unbiased root-mean-square difference; MAE: mean absolute error.

the TDS-1 satellite by the U.K. in 2014, it has brought new opportunities for land vegetation monitoring. Camps et al. [43] used TDS-1 GNSS-R data to study the sensitivity of SM on different types of surfaces, as well as extensive SM and NDVI values. SMAP, SMOS, and CYGNSS can also provide information on vegetation indices. Carreno-Luengo et al. [34] conducted the first GNSS-R global scale assessment experiment on SMAP satellite to study SM and biomass retrieval. Piles et al. [82] utilized SMAP vegetation optical depth and optical vegetation index, combined with RS technology, to provide a more accurate and comprehensive method for monitoring and predicting vegetation dynamics in agricultural ecosystems. Rodriguez-Alvarez et al. [83] analyzed the sensitivity of SMAP-R signals to growth-related characteristics of maize belt crops in the United States, studied the effects of crop type, vegetation water content (VWC), crop height, and vegetation opacity (VOP) on the signals, and

TABLE IV
CURRENT STATUS AND SUMMARY OF SPACEBORNE GNSS-R TECHNOLOGY VEGETATION PARAMETERS MONITORING RELATED WORK[1]

Vegetation Parameters	Literature	Satellites	Spatial Coverage	GNSS-R Observables	Reference Data	Auxiliary Data	Retrieval Models	Retrieval Accuracy
AGB and CH	Carreno-Luengo, et al. [84]	CYGNSS	Congo and Amazon rainforests	Reflected DWs ($WF_{r,raw}$), trailing edge width (TE), reflectivity (Γ)	ICESat-1/GLAS AGB	SMAP-derived VOD, PI, and SM	order polynomial "O" fit	There is a certain sensitivity to AGB up to ~350 and 250 ton/ha, respectively, over Congo and Amazon target areas, without an apparent saturation.
	Santi, et al. [65]	CYGNSS		Incidence angle, reflectivity and antenna gain	SMAP VOD	_	ANNs	R = 0.924, RMSE=0.1
	Santi, et al. [90]	TDS-1, CYGNSS		Reflectivity, SNR	ALOS2, SMAP VOD	_	ANN	R > 0.8, RMSE < 0.2
	Santi, et al. [85]	TDS-1, CYGNSS	Brazil (Manaus), Uruguay (Algorta), Alaska (Fairbanks), Finland, Argentina (Asuncion)	Reflectivity, SNR, Incidence angle, lon, lat	SMAP VOD, AGB Map, ICE-GLAS Tree Heights	ALOS-2	ANN	R ≈ 0.8, 37 t/ha ≤ RMSE ≤ 76 t/ha for local and global AGB retrievals (AGB in the range 0–400 t/ha), and 3.1 m ≤ RMSE ≤ 6.5 m for tree height retrieval (H in the range 0–45 m)
	Pilikos, et al. [89]	CYGNSS	Longitude: (-90°, -30°) Latitude: (-30°, 15°)	Max DDM, Mean DDM, Max Γ , mean Γ , SNR	ESA CCI biomass map	_	DL	R = 0.962, RMSE = 25.650 t/ha
	Chen, et al. [86]	CYGNSS	Quasi-Global	Traditional Reflectivity ($\Gamma_{surrface}$), Correction Reflectivity ($\Gamma_{LR}(\varepsilon_S,\theta_i)/\sigma_0^{coh}$)	AGB map derived from LUCID, ICESat/GLAS CH	SMAP SM	ANN	For AGB retrievals, RMSE = 64.84 Mg/ha, R = 0.80 in the range of 0 to 550 Mg/ha. For CH retrievals, RMSE = 5.97 m, R= 0.83 in the range of 0 to 45 m
Vegetation Optical Depth (VOD)	Pierdicca et al. [30]	CYGNSS	Brazil (Manaus), Uruguay (Algorta), Alaska (Fairbanks), Finland, and Argentina (Asuncion)	Reflectivity, SNR, DDM peak	SMAP VOD	MODIS NDVI	ANN	RMSE = 0.1, R = 0.924
VWC	Chen, et al. [91]	CYGNSS	Quasi-Global	The coefficient and intercept feature derived from the tau-omega model, land cover, lat, lon	SMAP VWC	SMPS SM, The land cover and NDVI derived from MODIS	Linear model and ANN	RMSE = 2.155 kg/m^2, R = 0.795 (The linear model); RMSE = 1.392 kg/m2, R ˜ 0.940 (The ANN model)

[1] VOD: vegetation optical depth, PI: polarization Index, NDVI: normalized difference vegetation index. σ_0^{coh} is the peak point of BRCS, $\Gamma_{LR}(\varepsilon_S,\theta_i)$ represents the surface Fresnel reflectivity.

discussed the possibility of correcting VWC and SM effects in electromagnetic signals using retrieval algorithms combined with GNSS-R measurements. Carreno-Luengo et al. [84] proposed a new GNSS-R method that combines CYGNSS data to study AGB detection in tropical rainforests, coniferous forests, arid forests, and humid forests. By analyzing the relationship between multiple observables of DDMs and AGB, the AGB of dense forest canopies was detected from a spaceborne platform. Santi et al. [85] pioneered the use of TDS-1 data to assess the sensitivity of GNSS-R observables to different forest parameters at the local scale, and then extended to the global scale using CYGNSS data, which confirmed the good sensitivity of GNSS-R data to target forest parameters (i.e., AGB, tree height, and VOD), and demonstrated the potential of GNSS-R in forest biomass monitoring. Chen et al. [86] proposed an improved retrieval method for AGB and canopy height (CH) based on CYGNSS observation data, SMAP data, and location. In spaceborne GNSS-R technology, there are differences in the polarization mode of receiver antennas among different satellites. The radar receivers in SMAP satellites use V and H linear polarization, while TDS-1 and CYGNSS satellites use LHCP antennas to receive reflected signals from the ground. Therefore, it is necessary to study the polarization application of GNSS-R in vegetation. The SMAP GNSS-R dataset is currently the most widely used GNSS-R dataset and the only dataset that provides GNSS-R polarization measurement data. Rodriguez-Alvarez et al. [87] demonstrated that the SMAP polarimetric GNSS-R reflectance derived from the mathematical formulation of Stokes parameters could enhance the radiometric data in dense vegetation areas, and pioneered the first polarimetric GNSS-R mission. Munoz-Martin et al. [88] used polarized GNSS-R data to analyze the correlation between Stokes parameters on land surface and SM, vegetation optical depth, and global forest CH, and estimated SM and vegetation optical depth using linear regression methods. This study provides a valuable dataset for future GNSS-R task design and explores the differences in polarization characteristics under different incidence angles and polarization directions. However, due to the complexity and diversity of vegetation, the use of spaceborne GNSS-R technology to retrieve vegetation indices is still in the exploratory research stage. Accurately understanding the microwave scattering mechanism of rough surfaces and vegetation parameters is the key theoretical basis for GNSS-R surface parameters RS. In future research, it is necessary to strengthen the research on GNSS-R RS theory modeling.

Table IV summarizes the work related to monitoring vegetation parameters using spaceborne GNSS-R technology in terms of observation satellites, spatial coverage, GNSS-R observations, reference data, validation data, retrieval models, and retrieval accuracy. These studies highlight the potential of spaceborne GNSS-R technology in retrieving forest biomass and related parameters. The analysis results also indicate that GNSS-R technology has better sensitivity compared to L-band radar, especially when dealing with high biomass values. The retrieval of forest parameters has been achieved using ANN combined with auxiliary data whenever possible. Specifically, SNR and incidence angle have been proven to be very helpful in improving retrieval accuracy.

Generally, existing work has confirmed the sensitivity of GNSS-R data to forest parameters and demonstrated encouraging retrieval performance. Considering that this may be the first attempt to use spaceborne GNSS-R data to retrieve forest biomass on a global scale, in the future, more reliable ground truth data, including the latest reference maps, should be

considered to evaluate the practical ability of GNSS-R in terms of spatial resolution. In addition, it is necessary to study the use of auxiliary information from other surface parameters (such as SM) to improve retrieval, as well as other observation values derived from DDM. Finally, more work should be done to fully utilize the synergistic effect between single base radar and GNSS-R.

Compared with marine applications, the research on spaceborne GNSS-R in the field of land RS is relatively lagging behind. Although spaceborne GNSS-R technology is feasible in vegetation monitoring [30], the research on vegetation parameters using spaceborne GNSS-R technology is still in the exploratory research stage, and currently mainly focuses on using spaceborne GNSS-R observation data to establish sensitivity analysis with vegetation parameters [43], [84], [85]. It is not only in the qualitative analysis research stage but also lacks the discovery of its underlying physical mechanisms, and there is still a certain gap from the quantitative retrieval of vegetation parameters. Therefore, the development and use of efficient and convenient retrieval algorithms will make this technology truly practical in vegetation RS, which is an inevitable development trend in the future [28]. There is a complex nonlinear relationship between spaceborne GNSS-R observations and vegetation parameters. Currently, using ML such as NNs to retrieve forest parameters is relatively easy because ML can simulate nonlinear relationships well and achieve good retrieval accuracy [65], [89].

It is worth noting that regarding the limitations of the current GNSS-R satellite, TDS-1 as a technical demonstration satellite has a smaller coverage range (and is currently out of operation), while the CYGNSS constellation has a wider coverage range, and is only limited to midlatitude regions. Absolute calibration issues, low power densities hitting the Earth's surface, and high variability of signals are other aspects that require further research to better utilize the technology on land. In the future, it is necessary to further explore more complex retrieval techniques based on NNs to comprehensively evaluate the actual differences in maturity and integrated product performance of GNSS-R compared to other Earth observation technologies (such as microwave radiometers). In the future, with the continuous improvement of datasets and tasks, we can expect that the potential and quality of biogeophysical parameters retrieval will be significantly improved, especially for parameters such as biomass, which are relatively immature and need to be studied more accurately.

V. Monitoring Freeze/Thaw Surface State Using Spaceborne GNSS-R

Soil freeze-thaw (F/T) is the process of repeated freezing and thawing of water in the soil, which is accompanied by a large exchange of water and heat that affects the energy and water balance at the surface, which is critical to the surface water cycle and is an important indicator of climate change [92]. In addition, soil F/T can also damage the soil structure, resulting in soil erosion and loss of soil nutrients, which in turn affects ecological balance [93]. Therefore, to better monitor climate change and protect the ecological environment, soil F/T conditions need to be monitored to obtain complete and detailed information on soil F/T.

Traditional single-point measurements of the F/T state of the soil, including temperature profile measurements and freezing tube measurements, often consume a lot of manpower and material resources, making it difficult for them to be widely applied. Optical RS, while allowing for wide-area observations, is susceptible to the limitations of cloud cover and weather conditions. Active microwave RS can provide high spatial resolution data but has a long revisit period and cannot update the changes in soil F/T status in a timely manner, while passive microwave RS, although it can provide all-weather monitoring capability, has a low spatial resolution of its products, which makes it difficult to clearly observe the changes in soil F/T. In recent years, with the rapid development of GNSS-R, it has been widely used in the ocean and land because the GNSS-R reflection signal is extremely sensitive to the water changes in the soil, and has the remarkable features of all-weather, near real-time, high-resolution (compared to passive microwave systems), which makes it possible to use GNSS-R reflection signal to observe soil freezing and thawing on a large scale. Due to the fact that GNSS-R reflection signal is extremely sensitive to SM changes and has the remarkable features of all-weather, near real-time, high-resolution, etc., which makes it possible to observe soil F/T on a large scale by using GNSS-R reflection signal, based on the above reasons, scholars in and out of China and abroad have carried out the research of observing soil F/T by using GNSS-R and have made a certain amount of progress in the research.

In 2014, Wu and Jin [94] used the wave synthesis technique to transform the soil F/T dielectric constant model into the Fresnel reflectivity model to obtain the linearly and circularly polarized reflectivity, and combined it with the GPS signal and the antenna's polarization information to obtain a fully forward multipath GPS simulator, and then observed the soil F/T changes in the observed values from the GPS simulator confirmed the viability of monitoring soil F/T via GNSS-R reflection signals. However, it should be noted that these results were solely based on simulations and lacked field verification. To verify whether SMAP data can be used for soil F/T observation, Chew et al. [95] analyzed the observation results of GPS reflection signals received by SMAP in high latitude areas in 2017 and compared them with on-site soil temperature data to quantify the changes in reflection signals during soil F/T. The seasonal changes in reflection signals proved the feasibility of using GNSS-R reflection signals to observe soil F/T conditions.

To further explore the sensitivity of GNSS reflection signals to soil F/T, Rodriguez-Alvarez et al. [96] used SMAP data in 2019 to classify the state of soil F/T in Alaska, and seasonally analyzed the state of F/T by considering different landscape categories and analyzed the effects of peak SNR, LES, trailing edge slope (TES), delay Doppler map average (DDMA), and polarization ratio (PR) corrected for vertical (V) and horizontal (H) polarizations on the soil freezing and thawing state, and the results show that the SMAP reflection signal is sensitive to the soil F/T state of different landscapes, and the most sensitive one is the peak SNR corrected by the V polarization; however, the experiment has deficiencies in data calibration and does

not take into account the satellite transmit power differences between them.

To study the effect of soil F/T state on DDMs and multipath information, in 2019, Wu et al. [73] extended the existing DDM simulation and analysis model and forward GPS multipath model to soil F/T monitoring, and simulated and analyzed the changes of DDM and multipath information when the soil F/T state transitions, and the results showed that the change of the surface dielectric constant would lead to a significant change of DDM as well as multipath information when soil freezing and thawing transition occurs. The results show that during soil F/T transition, the change of surface dielectric constant will lead to an obvious change of DDM and multipath information, so this change can be used to achieve the purpose of soil F/T monitoring, but the experiment only considered the case of bare land and did not consider the case of snow and vegetation cover.

Changes in the soil F/T status led to changes in the surface dielectric constant, which in turn affects the SR, and several scholars have carried out research based on this feature. For example, in 2020, Comite et al. [97] calibrated and analyzed the SR of TDS-1, and then observed the soil F/T state and compared the results with the SMAP data and the in situ soil data, showing that the height of the GNSS-R SR was related to the seasonal change, thus proving the feasibility of observing the soil F/T state by using SR, but the influence of the vegetation and water bodies caused anomalies in the SR of some areas, which affected the accuracy of detecting the soil F/T state. However, due to the influence of vegetation and water bodies, the SR in some areas is abnormal, which affects the accuracy of detecting the F/T status of soil. In 2021, Rautiainen et al. [98] conducted soil F/T observations in high latitude areas using calibrated TDS-1 SR data. This study was conducted at two scales:1) the land area of the Northern Hemisphere on a global scale, located between 55° and 80° north latitude; 2) the local scale at the FMI Sodankylä calibration and validation (cal/val) site. The observations were compared with the SMOS soil F/T data. The comparison of the two showed good agreement. This study confirms the sensitivity of GNSS reflections to soil F/T conditions and proposes a seasonal threshold detection method, which may pave the way for future operational products of the GNSS-R mission. However, challenges include insufficient data, measurement discontinuities, poor revisit times, and limitations in accurate calibration performance. In addition, the data are highly discrete and sensitive to vegetation cover and topography. Spaceborne GNSS-R sensors do not return to the same location on a regular basis and may produce variable reflections. In addition, incoherent reflections introduce speckle noise, which needs to be mitigated by an appropriate averaging strategy.

In order to further evaluate the capability of GNSS-R reflection signals to monitor soil F/T at high latitudes, Carreno-Luengo and Ruf [99] conducted soil F/T observations of the Andes and the Pampas grasslands based on the Seasonal Thresholding Algorithm (STA) using CYGNSS in 2022 and compared the results with the European Centre for Medium-Range Weather Forecasts (ECMWF). The results show that the soil F/T data detected based on this method matches well with ECMWF ERA5-Land and SMAP data, which confirms the feasibility of the algorithm for detecting soil F/T. However, only CYGNSS data are used to validate the algorithm, and there is a lack of other spaceborne GNSS-R data to further validate its algorithm.

The Tibetan Plateau is known as the "Roof of the World," and one of the most striking physical features is the freezing and thawing process of the soil. To study the feasibility of using CYGNSS to observe soil F/T in the Qinghai Tibet Plateau, Wu et al. compared and analyzed the F/T characteristics of SMAP with CYGNSS data from 2018 to 2020. The results showed that when F/T conversion occurs on the surface, changes in SR will lead to changes in the peak waveform of DDM. The relationship between CYGNSS SR and SMAP SM within the time series was also analyzed, and the results showed that the effect of SM on reflectance was small and negligible, and the F/T transition was the main factor affecting CYGNSS reflectance, proving that it is feasible to use the CYGNSS data for surface F/T monitoring on the Tibetan Plateau. It is worth noting that CYGNSS data quality is relatively poor in the Tibetan Plateau region due to the reduced certainty of mirror point capture at high altitudes [92]. In 2022, Carreno-Luengo and Ruf [100], [101] conducted soil F/T observations on the Tibetan Plateau based on STA using CYGNSS and compared the observations with data from the topography roughness index (TRI) and ECMWF ERA5-Land, and the comparisons showed good correlation. However, further exploration is needed to determine whether the STA algorithm can be applied to polar regions using data from the new GNSS-R high-inclination satellites. In the future, monitoring of polar regions can utilize GNSS-R data from the new generation of high-inclination satellites. Compared to traditional RS technology, GNSS-R has a higher spatiotemporal sampling rate, which can provide new insights and perspectives for monitoring highly dynamic F/T surface processes.

Current GNSS-R F/T studies are limited to a regional context, with time resolutions typically on a monthly scale and a lack of long-term F/T records. In addition, during the warm and cold transition seasons, the soil F/T state changes rapidly and the F/T cycle shows high heterogeneity, even switching several times in a short period of time. Accurate observation of the soil F/T cycle requires high spatial and temporal resolution. Therefore, there is a need to further explore spaceborne GNSS-R F/T detection capabilities. For this reason, as a complement to previous studies, in 2023, Yang et al. [102] used CYGNSS to make daily observations of soil F/T state on the Tibetan Plateau, which was different from previous studies in that the temporal resolution of the GNSS-R F/T study was successfully improved to the daily scale by introducing an ML (RF) method, whereas previous studies were often limited to seasonal or monthly scales. To demonstrate the reliability of the retrieval results, near-surface in-situ data were added for comparison. The results showed that compared with SMAP F/T data and in-situ data, the detection accuracy of CYGNSS reached 75.1% and 81.4%, respectively. The improved CYGNSS F/T retrieval results enable us to understand the spatial and temporal distribution and evolution of soil F/T in the Tibetan Plateau region in more detail, thus providing more information on temporal variability phenomena for short-term hydrological climate

TABLE V
RETRIEVAL APPROACH AND ACCURACY OF CURRENTLY PUBLISHED SPACEBORNE GNSS-R SOIL FREEZE–THAW DETECTION STUDIES[1]

Source	Satellites	GNSS-R Observables	Spatial Coverage	Temporal Resolution	Reference Data	Auxiliary Data	Validation Data	Retrieval Models (Methods)	Main Results
Comite et al. [97]; Pierdicca et al. [30]	TDS-1	Reflectivity	high latitude areas	Monthly scale	SMAP F/T	MODIS land cover classes	In Situ Data	–	The characteristics of decreasing reflectivity of frozen soil and increasing reflectivity of thawed soil, with a dynamic range of up to 10 dB and high spatial resolution (in the case of mainly coherent scattering, the spatial resolution is about a few kilometers)
Wu et al. [92]	CYGNSS	Reflectivity	Qinghai–Tibet Plateau	Daily scale	SMAP F/T	MODIS land cover classes	SMAP F/T	–	Proved the feasibility of using CYGNSS for surface F/T monitoring on the Qinghai Tibet Plateau
Carreno-Luengo and Ruf [99], [101]	CYGNSS	Reflectivity	Lat = [−35, −28]° and Lon = [−71, −67]°includes a region of the Andes; The Tibet Plateau (Lat = [25 37.5]°, Lon = [70 102]°), the Andes Mountains (Lat = [−37.5 −25]°, Lon = [−75 −65]°), and the Rocky Mountains (Lat = [35.537.5]°, Lon = [−109 −103]°)	Monthly scale	SMAP F/T	ERA5-Land SM and soil temperature	SMAP F/T	Seasonal-Threshold Algorithm (STA)	The CYGNSS F/T map of the target area shows consistency compared to the F/T product of the SMAP radiometer
Yang et al. [102]	CYGNSS	Reflectivity	Qinghai–Tibet Plateau	Daily scale	SMAP F/T	SMAP surface roughness coefficient, and VOP	SMAP F/T	RF	The F/T retrieval accuracy of CYGNSS was 75.1% and 81.4% (vs. SMAP data and data from independent in situ stations)
Yang et al. [103]	CYGNSS	Reflectivity	Quasi-Global	Daily scale	SMAP soil F/T cycle	SMAP VOP	ISMN and NCDC hourly dataset	RF	The F/T retrieval accuracy of CYGNSS was 95.5% and 82.0% (vs. SMAP data and data from independent in situ stations)
Wu et al. [104]	FY- 3E	Reflectivity	Arctic Circle	Seasonal scale	SMAP F/T	SMAP SM, soil texture, soil temperature, soil bulk density, MODIS land cover and land use map	SMAP F/T	STA	There is strong consistency between the SR ratio factor and the SMAP F/T value, and the accuracy of the F/T retrieval algorithm exceeds 60%

[1]ISMN: International SM Network. NCDC: National Climatic Data Center.

studies. However, the poor resolution of gridded data makes it difficult to accurately detect changes in soil freezing and thawing within the grid. In 2024, Yang et al. [103] proposed a daily F/T detection scheme combining GNSS-R reflectivity and minimal ancillary data for quasi-global daily F/T retrieval. By selecting the minimum amount of auxiliary data, the dependence on other external data is reduced. In addition, the performance of the F/T retrieval results was assessed using SMAP data and independent in situ data. The results showed that the F/T retrieval accuracy of CYGNSS was 95.5% and 82.0%, respectively, when comparing SMAP data and independent field site data. Considering the high spatiotemporal coverage of CYGNSS F/T results, compared with actual SMAP observations, its coverage on the daily scale has increased by 23.3%. In addition, by filling the gaps in SMAP data, CYGNSS data effectively improved the SMAP F/T sample interval and increased accuracy by 26.0%. Of particular note is the monthly performance-based F/T accuracy of 85.1% for the combination of CYGNSS and SMAP, and a 20.5% improvement over the existing SMAP daily F/T product. Overall, the quasi-global daily F/T results obtained based on CYGNSS and SMAP measurements can provide a meaningful addition to existing databases with clearly defined accuracy. This demonstrates that high precision and time-resolved F/T products can be generated from spaceborne GNSS-R and SMAP radiometer measurements. As given in Table V, several main aspects are summarized and compared, including the observation satellites, the GNSS-R observations, the main components of the reflected signal, the spatial coverage, the spatial resolution, the reference data, the ancillary data, the validation data, the retrieval model, and the specific details of the main results.

Recently, Wu et al. [104] demonstrated for the first time the potential of the FY-3E GNOS-R payload to detect the freeze/thaw (F/T) state of near-surface soils at high latitudes (especially the Arctic Circle), using GNSS-R observations from DOY179 in 2021 to DOY270 in 2022 data and using SR ratio factors to distinguish F/T changes. Comparison with SMAP F/T products shows strong consistency between the SR ratio factor and SMAP F/T values, with the accuracy of the F/T retrieval algorithm exceeding 60%. The use of GNSS-R reflection signals to monitor the F/T state of soil is a promising technique, but it also faces many challenges. Wet snow cover makes detection of soil thawing difficult, low reflectance is often misinterpreted as a frozen condition, and increased reflectance during thaw can indicate that the snow cover is subsiding, with the aid of ancillary data. Further research needs to consider the footprint areas and scattering properties of different target surfaces, including the effect of incidence angle changes, and consider ML methods to compensate for disturbances. Given the inherent limitations of the dependent dataset, especially considering that discontinuous data can only be obtained from a single satellite platform, existing research analysis shows that using aircraft with appropriate orbital inclinations, based on GNSS-R missions that only receive small satellite constellations, can provide the required coverage and modification time. In this context, the currently launched Chinese BF-1 A/B, FY-3E/3F/3G, and TM-1, as well as the

HydroGNSS mission under development, will help to overcome most of the existing limitations and provide larger and more reliable datasets.

VI. Flood Detection Using Spaceborne GNSS-R

A clear and intuitive understanding of flood events is important for the stable development of societies, and despite the myriad of RS technologies available for mapping surface floods, there are still gaps in the ability to rapidly map flood inundation at the required temporal resolution for understanding how floods evolve. Although traditional manual flood measurement methods have high accuracy, they are time-consuming, labor-intensive, and costly. Moreover, if the flood is relatively turbulent, this method also poses certain risks. Although optical RS can map flood inundation areas on a large scale, it is only suitable for open and unobstructed areas and has certain limitations in mapping floods with vegetation cover. Active microwave RS offers high spatial resolution, yet its long revisit period and the inability to update flooding dynamics of flooding in a timely manner means that it is fortuitous in capturing flood events. Consequently, it is deficient in observing changes in the extent of flood inundation. Whereas passive microwave RS can provide all-weather monitoring capability, its products have low resolution and do not provide a clear understanding of the detailed aspects of flood events [105], [106]. As a new RS detection technology, GNSS-R has unique advantages such as global coverage, low power consumption, abundant signal sources, and low cost, and GNSS reflection signals are highly sensitive to water bodies [107], [108], which makes it possible to monitor large-scale floods using GNSS-R reflection signals. Currently, domestic and foreign scholars have conducted research on using GNSS-R reflection signals to detect floods and have achieved certain research results.

To better detect flood-related information, many scholars retrieve floods by constructing models. In 2012, Beckheinrich et al. constructed a phase model using GPS reflection signals to calculate the average water level height. They combined coherent observations and then used the least squares method to extract the minimum slope to calculate the water level height. The experimental results showed that the average water level height reached the level of decimeters but only GPS signals were used, resulting in a single signal source and low retrieval accuracy of the model, making it difficult to describe flood events in detail [107], [109]. In 2020, Chew and Small [110] proposed a forward model to describe how the SR of CYGNSS varies with different types of floods. The results showed that the relationship between SR and flood range heavily depends on the surface roughness of land and water. The rougher the surface, the easier it is to detect flood inundation range. However, this model is only applicable to areas with high surface roughness and has poor performance in areas with smooth surfaces. In 2022, Wilson-Downs et al. [111] used a coherent scattering model to measure the range of surface water. This model can simulate the complex shape of water bodies and the coherent power of surface roughness, accurately detecting the inundation range of surface water. However, it did not consider the situation of water bodies with vegetation coverage, so it has certain limitations in detecting water bodies in complex situations. In the same year, Song et al. [112] proposed the dual-branch NN model, comprising two components: CNN and backpropagation NN. This model combines the physical features of GNSS-R with the abstract features mined by the CNN for better flood retrieval. However, this model is not very accurate in flat areas because it does not take into account the effect of land topography. The models proposed by the above-mentioned scholars have all improved the accuracy of flood retrieval to a certain extent and expanded the methods of flood retrieval. However, due to the centralized use of GPS reflection signals received by the CYGNSS satellite, the signal source is relatively single, and the model itself has certain shortcomings, which have not considered flood detection in complex situations. Therefore, it is unable to retrieve more information about floods, such as flood depth, flood velocity, and flood flow rate [31]. It is necessary for follow-up studies to consider the use of multiple data fusion methods to construct flood retrieval models and to improve model retrieval algorithms to improve flood retrieval.

To further improve the accuracy of flood detection, many scholars carry out research on flood detection using relevant algorithms. In 2019, Rodriguez-Alvarez et al. [113] used the multidecision tree randomization (MDTR) algorithm combined with GNSS-R signals to classify tropical wetland floods. The experimental results showed that the algorithm can detect floods under dense vegetation cover, which can be extended to characterize biological communities. Due to the algorithm mainly combining CYGNSS data and the relatively single training samples, the accuracy of detecting floods under vegetation cover is not high. In 2020, Ghasemigoudarzi et al. [114] used the Random Under Sampling Boost (RUSBoost) classification algorithm based on CYGNSS to detect mountain floods. They observed floods by extracting LES, TES, and SNR data and compared the detection results with those of SVMs. The results showed that the flood detection accuracy based on the RUSBoost algorithm was higher but it was only suitable for large-scale mountain floods, and the effect was not good for small-scale mountain floods. In 2022, De Tarso Setti et al. [115] proposed a trajectory-based algorithm that uses CYGNSS data to plot the seasonal inundation range of the Pantanal wetland. The detection results were compared with the global surface water detector (GSWE) products and surface water microwave product series (SWAMPS), and the results showed that the algorithm has higher accuracy in detecting water bodies. However, the algorithm only takes into account the effect of signal power and angle of incidence, whereas the factors affecting flood detection are diverse, and thus the algorithm itself is not perfect. In 2023, Chew et al. [116] proposed a flood inundation detection algorithm based on CYGNSS data, which first parameterizes the data on soil surface, water body roughness, and SM, and then retrieves the extent of flood inundation using a dielectric model combined with reflectance. The algorithm cannot be applied to a wide range of areas due to the uncertainty of the data on which the parameterization is performed. Although the above algorithm can detect the range of floods, the algorithm itself has poor generalization ability, which makes it difficult to be applied to the

detection of floods in complex situations, so the improvement of the algorithm is an urgent problem that needs to be solved before the application of this technology to flood monitoring.

Previous studies have confirmed that spaceborne GNSS-R reflection signals are highly sensitive to floods, and changes in floods can lead to changes in GNSS-R SR [115]. Therefore, many scholars have flood detection based on the correlation between floods and SR (i.e., the SR observation threshold approach). In 2018, Chew et al. [79] utilized CYGNSS SR data and then used the SR thresholding method to map the extent of flood inundation and compared the results to SMAP data, which showed that CYGNSS was able to observe higher resolution flood data than SMAP. Although the flood inundation range was detected based on the SR data, different thresholds yielded different inundation ranges, so the thresholds had to be determined according to the actual needs. In 2020, Rajabi et al. [117] used a two-base radar equation formulation to calculate the SR and then retrieved the flood areas based on the SR and compared the results with the MODIS data, which showed that the flood data retrieved based on the SR had a high correlation with the MODIS data, and that the flood data detected based on the SR could be used as a supplement to the existing flood products. In 2021, Zhang and Yang used CYGNSS SR to observe floods in Henan Province and compared the results with SMAP data. The results showed that flood observation based on SR had higher resolution [118], [119]. In 2023, Downs et al. [120] quantified CYGNSS flood observations using a simple thresholding approach and compared them with VIIRS, MODIS, and Sentinel-1 data, which showed that CYGNSS has a higher accuracy in detecting floods and can be used as a supplement to existing flood products. In the same year, Yang et al. [121] proposed the Annual Threshold Flood Inundation Index (ATFII) to implement flood inundation rate retrieval based on CYGNSS data and validated the results using VIIRS and GPM data. The results indicate that ATFII cannot only perform flood inundation retrieval but also quantify flood inundation levels. However, the imperfect matching of the VIIRS grid and CYGNSS data at the spatial scale resulted in reducing the accuracy of the ATFII retrieval of floods. Subsequently, Wei et al. [122] also confirmed the feasibility of the method when using CYGNSS SR to detect floods in Guangdong Province, and the detected flood data had higher accuracy compared to SMAP data. The above-mentioned scholars utilized the SR threshold method, although it was successful in detecting surface flooding. However, the choice of threshold may vary depending on parameters such as topography, roughness, and vegetation. Therefore, there may be differences in the choice of thresholds under different environmental conditions [123], [124].

The SR measured by spaceborne GNSS-R can be calculated using the following formula. The total scattering power P_{rl} of the bistatic radar can be determined as follows:

$$P_{rl} = P_{rl}^{c} + P_{rl}^{i} \tag{7}$$

where P_{rl}^{c} and P_{rl}^{i} can be expressed as

$$P_{rl}^{c} = \frac{P_r^t G^t}{4\pi (R_{ts} + R_{sr})^2} \frac{G^r \lambda^2}{4\pi} \tau_{rl} \tag{8}$$

$$P_{rl}^{i} = \frac{P_r^t G^t G^r \lambda^2}{(4\pi)^3 R_{ts}^2 R_{sr}^2} \sigma_{rl} \tag{9}$$

where P_{rl}^{c} and P_{rl} represent coherent reflection power and incoherent scattering power, respectively;P_r^t is the transmission power of the GPS satellite antenna;G^t is the gain of GPS satellite antenna; G^r is the gain of the CYGNSS antenna;R_{ts} is the distance from the GPS satellite to the mirror reflection point; R_{sr} is the distance from the mirror reflection point to the CYGNSS receiver; τ_{rl} represents SR; σ_{rl} is the bistatic radar cross section (m^2). λ is GNSS signal wavelength.

When using the CYGNSS reflection signal to draw water bodies, it can be assumed that the reflection signal is mainly coherent reflection, and formula (8) can be converted into the form

$$\begin{aligned} 10\log P_{rl}^{c} = {} & 10\log P_r^t + 10\log G^t + 10\log G^r + 20\log\lambda \\ & + 10\log\tau_{rl} - 20\log(R_{ts} + R_{sr}) - 20\log(4\pi) \end{aligned} \tag{10}$$

then SR is

$$\begin{aligned} \mathrm{SR} = 10\log\tau_{rl} = {} & 10\log P_{rl}^{c} - 10\log P_r^t - 10\log G^t \\ & - 10\log G^r - 20\log\lambda + 20\log(R_{ts} + R_{sr}) + 20\log(4\pi). \end{aligned} \tag{11}$$

Since DDM is affected by the angle of incidence, the correction for the angle of incidence is

$$\mathrm{SR} = \mathrm{SR} - 10\log\cos^n\theta \tag{12}$$

where θ is the incidence angle, and n is the correction coefficient, which is generally taken as 1.

In addition to the above-mentioned methods, many scholars have carried out studies on flood detection using SNR, LES, TES, and coherent signals. In 2018, Jensen et al. [126] used SNR, LES, and TES observations from CYGNSS DDM to detect floods and compared them with synthetic aperture radar (SAR) detection results. The results showed that SNR observations had higher sensitivity to surface water compared to SAR, but due to the rough signal analysis and processing, it was not possible to accurately quantify the surface water range [125]. In 2021, Zeiger et al. [127] used CYGNSS SNR to detect changes in river water levels and compared the results with ocean sensor data. The results showed that SNR-based detection had higher accuracy, but due to the use of only CYGNSS data, it was not effective for large rivers. In 2022, Wang et al. [128] applied a power ratio to identify changes in DDM coherence in inland water bodies and compared the results with the DDM power-spread detector (DPSD). The results showed that using a power ratio to detect water bodies had higher accuracy, but due to the generation of incoherent scattering signals on rough surface water surfaces, it was not effective in detecting large lakes. In 2023, Wang et al. [129] used the L2P/L2W reflection signals of GPS to detect the water level, and the observation results can reach centimeter-level accuracy on the calm water surface, while the accuracy is poor for the fluctuating water surface due to the imperfect processing of the signals. The above-mentioned analyses show that these methods have certain limitations and are difficult to widely apply to flood monitoring, so it is necessary to

TABLE VI
RETRIEVAL APPROACH AND ACCURACY OF CURRENTLY PUBLISHED SPACEBORNE GNSS-R FLOOD DETECTION STUDIES[1]

Source	Satellites	GNSS-R Observables	Spatial Temporal Coverage	Temporal Resolution	Reference Data	Auxiliary Data	Validation Data	Retrieval Models (Methods)	Main Results
Chew et al. [79]	CYGNSS	Reflectivity	The southeastern United States and Caribbean	~3 days	SMAP	–	SMAP	Threshold method based on SR observations	Compared with SMAP radiometers, CYGNSS data provides clear signals of land surface saturation and inundation with higher spatiotemporal resolution.
Wan et al. [123]	CYGNSS	Reflectivity	China	Daily scale	SMAP	SMAP/SMOS-Derived Brightness Temperature; GPM precipitation	SMAP	Threshold method based on SR observations	CYGNSS has the ability to monitor flood inundation dynamics and obtain flood inundation areas.
Ghasemigoudarzi et al. [114]	CYGNSS	Eleven different observables [2]	Hurricane Harvey and Hurricane Irma	–	DFO flood maps	SRTM90m DEM; Wetland V3 data provided by the CIFOR; GSW Occurrence data	DFO flood maps	RUSBoost	For Hurricane Harvey and Hurricane Irma, the selected method is able to detect 89.00% and 85.00% of flooded points, respectively, with a resolution of 500m × 500m, and the detection accuracy for non-flooded land points is 97.20% and 71.00%, respectively.
Chew and Small [110]	CYGNSS	Reflectivity	Amazon Basin and Lake Eyre, Australia	Every two weeks	Landsat 8 MNDWI	SMAP roughness values and SM	Landsat 8 MNDWI	Modeling heterogeneous footprints	The sensitivity of reflectivity to inundation is greatest for rough surfaces; SM confounds the inundation signal for smooth surfaces.
Rajabi et al. [117]	CYGNSS	SNR	Sistan and Baluchestan province	Three days (13 January to 15 January 2020)	MODIS false-color images	–	MODIS false-color images	SNR Threshold	The estimated area of the flooded area is approximately 19644 km2, accounting for 10.8% of the province's total area. The flood risk is higher near depressions, lakes, and coastal areas.
Zhang, et al. [119], [132]; Yang, et al. [118]; Wei, et al. [122]	CYGNSS	Reflectivity	Henan Province and Guangdong, China	five days; daily scale	SMAP	DEM; SMAP SM; GPM and meteorological stations precipitation; RS monitoring data of land use in Henan Province in 2020; CLDAS-v2.0 daily precipitation data; Sentinel-2 L2A data	SMAP; MODIS	Threshold method based on SR observations	The flood range retrieved by CYGNSS is consistent with the range retrieved by the SMAP and MODIS, as well as the precipitation data retrieved and measured by GPM and meteorological stations. However, due to the low spatiotemporal resolution of SM in SMAP, some detailed information about the inundation range may be lost.
Chew et al. [116]	CYGNSS	Interpolated reflectivity observations	Amazon, Mozambique, Mali, and Australia	three days	–	global surface water dataset derived from Landsat data, a static dataset of AGB, SMAP SM	surface water data including SWAMPS, PALSAR-2, Dartmouth Flood Observatory, MODIS, and the Global Surface Water Explorer	Reflectivity model	Inundation maps produced with CYGNSS data correspond well to validation maps. However, the differences stem from calibration errors, inaccuracies in models and auxiliary data, among which parameterization of SM and water surface roughness often leads to underestimation of inundation scores relative to other surface water products, especially in areas with higher surface water ranges.
Downs et al. [120]	CYGNSS	normalized SNR	South Sudan	Month scale	VIIRS flood product	–	MODIS, and Sentinel-1	Threshold method based on NSNR observations	Compared to Sentinel-1 data, CYGNSS measurement provides improved performance and the ability to detect floods caused by optical technology failures. The proposed method detected 35.4% more surface water than Sentinel-1, while products based on VIIRS and MODIS underestimated 4.8% and 83.7%, respectively.
Yang et al. [121]	CYGNSS	Surface reflectivity calibrated by vegetation and surface roughness	southeast China	Daily scale	VIIRS floodwater fraction data	SMAP brightness (TB) 9 km gridded data	VIIRS flood product and GPM precipitation data, SMAP SM	ATFII	For monthly results, the R value between VIIRS flood products and ATFII varies between 0.51 and 0.64, with an acceptable level of significance ($p<0.05$); ATFII can retrieve flood inundation and quantify flood change levels on a fast time scale; ATFII is consistent in quality with VIIRS flood products, GPM-derived precipitation, and SMAP SM, and can provide high-precision spatiotemporal distribution of flood inundation.
Li, et al. [133]	CYGNSS	High sampling rate complex DDM reflected by Beidou-3	Mississippi River	–	Sentinel-2	–	–	Coherent Coefficient	The reflection measurement of Beidou-3 shows the potential for detecting surface water under thick vegetation canopy (up to 300 Mg/ha), which can supplement the existing observation network.
Ma et al. [130]	CYGNSS	Reflectivity calibrated by physics-based algorithms	Pakistan	Three days	Tb and SM data for SMAP and SMOS	MODIS data; GPM precipitation maps; Land cover	Sentinel-1 GFM observed water extent (OWE) data; SMAP/SMOS Wf	surface water fraction (Wf) Retrieval Method	The average overall retrieval accuracy of CYGNSS was approximately 64.44% and the average overall commission error was approximately 17.78%.

[1]GPM: global precipitation measurement, RUSBoost: random under-sampling boosted classification algorithm; SRTM90m DEM: shuttle radar topography mission digital elevation model; CIFOR: Center for International Forestry Research; GSW: global surface water; MNDWI : modified normalized difference water index; DFO: Dartmouth flood observatory; VIIRS: visible infrared imaging radiometer suite; GFM: global flood monitoring.

[2]A total of 11 different observables including corrected signal to noise ratio (SNR), trailing edge slope (TES), leading-edge slope (LES), delay-Doppler map average (DDMA), the width of the waveform (Wave-width), the first generalized linear observable (GLO),kurtosis, maximum, mean, skewness, and variance are extracted for each SP.

deepen the research on the analysis and processing of reflection signals to seek a more perfect reflection signal analysis and processing method to improve the accuracy of flood detection. As given in Table VI, summaries and comparisons are made in several main areas, including observing satellites, GNSS-R observables, spatial coverage, temporal resolution, reference data, ancillary data, validation data, retrieval models (or methods), and specific details of the specific results.

In summary, spaceborne GNSS-R technology has demonstrated great potential and unique advantages in flood monitoring and has achieved some remarkable results. However, this technology is still immature in flood monitoring. At present, there are mainly the following problems.

1) The spaceborne GNSS-R observation data used are mostly GPS reflection signals received by the CYGNSS satellite. Due to the relatively single data source, flood information cannot be detected in complex situations, such as flood coverage, flood intensity and depth, water body characteristics and hydrodynamics, and surface characteristics and coverage factors.

2) Although recent work by Ma et al. [130] has considered the impact of factors such as topography, surface roughness, and vegetation coverage on flood monitoring accuracy, the uncertainty of modeling parameters and auxiliary data errors will also limit flood monitoring accuracy.
3) The quasi-randomly distributed nature of CYGNSS sampling leads to gaps in the daily observations. Although the previously observed behavior interpolation (POBI) method has been used to address this well-known problem, this similar interpolation inevitably leads to some errors in the results. Another limitation is the availability of the surface water fraction (Wf) reference dataset. Although there are some RS-based inland water dataset, most provide static inland water data from historical observations. Due to the limitations of RS satellite working mechanisms (band, spatiotemporal resolution) and observation conditions (clouds, rain, vegetation), there is currently no globally available, spatiotemporal continuous, and high-frequency updated dataset for inland water bodies. Although existing studies use the high-resolution Sentinel-1 spaceborne water body dataset global flow monitoring (GFM) as validation data, the weakness of GFM to provide only open water soundings leads to overestimation of CYGNSS Wf retrieval results in some areas. However, the long revisit period limits the application of GFM in monitoring highly dynamic flood events.

Currently, The Global Constellation Observing System for Meteorology, Ionosphere, and Climate (COSMIC) Data Analysis Archive Center website provides free access to the available CYGNSS GNSS-R dataset covering flood events. Users interested in this dataset can visit: https://data.cosmic.ucar.edu/gnss-r/inundation/cygnss/ in order to download the CYGNSS flood map (3 km EASE-2 grid), these maps are currently available for the period from March 20, 2017 (DOY: 079) to June 30, 2022 (DOY: 181). However, users should be cautious when using retrieval results for hydrological analysis and pay attention to the uncertainty and drawbacks of the current form of retrieval results [116]. Incorporating several sources of inundation maps into one's interpretation of inundation dynamics is likely to be more informative than using one source of data alone.

In the future, the focus should be on developing flood monitoring algorithms based on multifrequency and multiconstellation GNSS reflection signals, ultimately obtaining clearer and more intuitive global high spatiotemporal resolution flood maps, and providing effective data support for flood control and policy formulation. In the future, the following aspects should be focused on: 1) Polarimetric GNSS-R, such as HydroGNSS, as it is expected to support detection of flooding under vegetation; 2) SAR/GNSS-R data fusion/integration in order to get the advantage of the very different acquisition geometries (backscattering versus forward-scattering) [131]; 3) developing flood monitoring algorithms based on multifrequency and multiconstellation GNSS reflection signals, ultimately obtaining clearer and more intuitive global high spatiotemporal resolution flood maps, providing effective data support for flood control and policy formulation. Meanwhile, the release of more RS data focused on surface water detection will provide more datasets to choose from. The cross validation of CYGNSS retrieval of inland water bodies with these datasets and the fusion of multisource RS data to obtain higher spatiotemporal resolution surface water monitoring results must be the focus of future research.

VII. Detecting Inland Water and Monitoring Wetland Dynamics Using Spaceborne GNSS-R

A. Detecting Inland Water

Inland water bodies are those that exist on land, including lakes, rivers, reservoirs, marshes, and ponds. Compared to the oceans, inland water bodies are usually smaller in size and are more susceptible to direct impacts from human activities and the natural environment. However, due to the impacts of human activities, such as water pollution, overexploitation of water resources, and degradation of wetlands, inland water bodies face many challenges and require conservation and management measures to maintain their sustainability. The advent of spaceborne GNSS-R provides a method for inland water monitoring [134].

Measurements made by the GNSS-R instrument show that the reflected power in inland waters is very strong, which is attributed to coherent scattering from the first Fresnel zone. CYGNSS is designed to estimate wind speeds over the oceans, and it is also highly sensitive to inland waters [135]. Mapping inland water bodies is a challenging task due to the complex variations in topography and water surface features [136]. In inland water scenes, the CYGNSS DDM shows very high peak reflected power and limited delay and Doppler spread. The SNR of the actual CYGNSS-measured reflected signals varies greatly because the CYGNSS signal on land is affected by surface type and roughness, soil and VWC, and vegetation density. Therefore, it is very difficult to capture global water bodies, especially small water bodies, using only threshold methods. To address this problem, Gerlein-Safdi and Ruf [137] proposed an algorithm to remove and process CYGNSS SNR data and generate reliable global water masks over the latitudinal range of CYGNSS coverage from approximately 40° N to 40° S to identify to map and resolve the location of inland bodies of water, such as lakes and rivers, with respect to the changes. Loria et al. [74] presented the development of a forward model for coherent scattering over inland waters with the aim of evaluating the accuracy of a wetland-wide retrieval algorithm applied to CYGNSS data over land. GNSS-R reflectometry over inland waters shows strong coherent scattering. Strong reflection signals generated over smaller spatial scales (several kilometers) are sensitive to surface wave height. This sensitivity can be used to estimate wave height profiles in inland waters. In combination with wind and wave modeling, wind vector retrieval can be performed using forward modeling methods. Loria et al. [138] pioneered the retrieval of wind vectors and wave heights in inland waters using spaceborne GNSS-R. This study used a passive bidirectional radar receiver on CYGNSS to estimate the surface wave profiles and wave heights in inland waters. The study used a passive

bidirectional radar receiver on CYGNSS to estimate the surface wave profiles and wind vectors of inland water bodies. The results showed that the coherent signal is highly sensitive to surface roughness and the total reflected power is also sensitive to the wave height profile. When considering large water bodies, the number of data points collected for water content is much less than the number of data points acquired from land, resulting in an unbalanced dataset. Integrated classifiers are combinations of basic classifiers, and various balancing methods can be applied to the integrated approach and different algorithms have been developed based on them. Ghasemigoudarzi et al. [139] implemented a high-resolution ML method for detecting inland water content using CYGNSS data by means of the RUSBoost algorithm. Kossieris et al. [140] detected inland water bodies using unsupervised ML algorithms. In 2023, Carreno-Luengo et al. [141] used CYGNSS Raw IF data to study the detection of inland water bodies, and the results showed that the use of CYGNSS Raw IF data is promising for detecting small inland water bodies. A new CYGNSS data product that accurately detects fully and partially coherent scattering and provides information on the intensity of the scattering signal for better application in application areas such as surface water monitoring is also provided. However, wind may increase the roughness of inland water bodies, such as large lakes [142]. When the roughness of a surface increases, its reflections become more incoherent. Distinguishing between water and land in such situations is more challenging and requires further research. The detection of future changes in water level dynamics is also worth investigating. As given in Table VII, it is mainly summarized and compared from several aspects, including observation satellite data, GNSS-R observables, spatial coverage (resolution), reference data, retrieval models (or methods), and specific details of the main results. In the table, NBRCS represents normalized BRCS.

B. Monitoring Wetland Dynamics

Wetlands are areas of land that are covered or saturated with water for a certain period or continuously, including marshes, rivers, lakes, coastal wetlands, and artificial wetlands. Wetlands are unique and rich environments in ecosystems with important ecological functions and values. Wetlands are one of the major sources of atmospheric methane, and methane emissions from wetlands are influenced by a variety of factors, including wetland type, water level, temperature, vegetation type, and human activities. Therefore, accurate assessment and monitoring of wetland methane emissions is critical to understanding the atmospheric methane cycle and the impacts of climate change.

At L-band frequencies, the roughness of typical ocean and land surfaces can cause diffuse reflection of GNSS signals. However, the surface of wetlands and other inland water bodies is usually very smooth, which allows them to generate coherent reflections [108]. Nghiem et al. [157] proposed that GNSS-R can identify flooded wetlands even under dense vegetation cover. GNSS reflectometers are sensitive to wetland changes, but quantitatively formulating the geophysical products of wetland reflections remains a challenge. Zuffada et al. [158] used reflection datasets from SMAP radar receivers to demonstrate the sensitivity of reflections to small surface features and their seasonal variations, and proposed an algorithm for wetland type classification. Jensen et al. [126] assessed the ability of spaceborne GNSS-R to characterize surface inundation dynamics in a tropical wetland complex with a combined analysis of contemporaneous L-band SAR, GNSS-R, and ground-based measurements. The potential of spaceborne GNSS-R technology in inland water and wetland monitoring has been demonstrated in previous studies by analyzing data from TDS-1 and CYGNSS missions [79], [157], [159], [160]. Rodriguez-Alvarez et al. [113] proposed a method for classifying tropical wetland floods using observable data obtained from GNSS-R measurements and auxiliary data and demonstrated the utility of GNSS-R observable values from CYGNSS data and auxiliary datasets in describing wetland inundation. Morris et al. [161] proposed a new approach to monitoring wetland dynamics using CYGNSS and developed a mapping method for wetland inundation using CYGNSS data by matching Everglades depth estimation network (EDEN) bathymetry estimates using Everglades as a case study. The results show that CYGNSS is capable of observing wetland dynamics in the tropics frequently and with high resolution on short time scales. Arai et al. [162] developed a reliable method for assessing the spatial and temporal dynamics of tropical wetland inundation by proposing a new quality control technique called "accuracy index" using available GNSS-R data. CYGNSS observations are sensitive to variations in incidence angle and estimated GNSS transmitter power, which can lead to errors in the classification algorithm. Setti et al. [115] proposed a new method for generating inundation maps and estimating the inundation range using CYGNSS GNSS-R data, which removes the effects of GNSS transmit power and incidence angle. Zeiger et al. [163] mapped the watershed extent of tropical wetlands by weekly time sampling using spaceborne GNSS-R technology in order to resolve the current uncertainty about the watershed extent of tropical wetlands and to provide time-series data on the watershed extent of wetlands globally. Downs et al. [164] proposed an algorithm for predicting water depth and surface water range based on CYGNSS observation data, and preliminarily evaluated its ability to observe inland water range, depth, and daily time-scale depth changes. The results show that the SNR of CYGNSS is highly correlated with the depth and extent of shallow vegetated waters, providing a potential solution to the limitations of traditional RS methods. GNSS-R technology (particularly the CYGNSS) has shown great potential for monitoring surface water under dense vegetation and clouds. Downs et al. [165], [166] combined CYGNSS data, ancillary information, and modeling to predict inundated areas under vegetation and create seasonal maps. The ability of CYGNSS to discriminate between different vegetation types was verified through comparison with validation data and other RS methods. In situ methods for wetland monitoring can be supplemented by utilizing the high observation frequency and undervegetation observation capability of CYGNSS. Table VIII summarizes and compares several main areas, including observational satellite data, GNSS-R observables, spatial coverage, ancillary data, reference data, retrieval models (or methods), and specific details of the main results.

TABLE VII
RETRIEVAL APPROACH AND ACCURACY OF CURRENTLY PUBLISHED SPACEBORNE GNSS-R INLAND WATER DETECTION STUDIES[1]

Source	Satellites data	GNSS-R Observables	Spatial Coverage (Resolution)	Reference Data	Retrieval Models (Methods)	Main Results
Gerlein-Safdi and Ruf [137]	CYGNSS	Reflectivity	0.01° × 0.01°	MODIS watermask product	An image processing algorithm	This algorithm can be used to draw short-term maps using monthly or seasonal data to monitor short-term hydrological phenomena such as seasonal floods.
Li et al. [143]	TDS-1, CYGNSS raw IF data	SNR	–	–	–	This study demonstrates the potential of GNS S-R technology in monitoring extremely dense wetlands on satellite platforms.
Ghasemigoudarzi et al. [139]	CYGNSS	SNR, kurtosis, maximum, and variance	Congo and Amazon basins (0.01° × 0.01°)	Global Surface Water data	RUSBoost	The proposed method can detect 95.4% and 93.3% of water bodies in the Congo and Amazon watersheds, respectively. For the Congo and Amazon basins, the water detection accuracy of the RUSBoost-based classifier has improved by 3.9% and 14.2% respectively compared to the inland water detection method based on image processing.
Loria et al. [74]; Zavorotny et al. [142]	CYGNSS raw IF data	SNR	Amazon river, Lake Ilopango	MODIS watermask data	SNR method	When designing a retrieval algorithm for drawing wetland area maps, consideration should be given to the changes in peak reflection power of inland water bodies caused by scene heterogeneity.
Al-Khaldi et al. [144]	CYGNSS	Power ratio (PR), SNR	Global (from 1 to 3 km)	Landsat water masks	Threshold method based on PR and SNR	Compared to Pekel water masks from Landsat images, the probability of accurately detecting many water bodies of interest exceeds 80%.
Morris et al. [145]	CYGNSS	Normalized SNR	–	EDEN water depth product	Logistic regression model	The estimation of surface water probability by CYGNSS also has corresponding uncertainty, which can be used to integrate CYGNSS data with other observation data.
Wilson-Downs et al. [111]	CYGNSS	Normalized SNR	Amistad reservoir	Binary water mask formed from landsat images	SNR method	This method has the potential to reliably detect changes in the surface water range below 4 square kilometers, corresponding to a 3% in-crease over the baseline extent.
Yan et al. [146]	CYGNSS	refletivity	Amazon and Congo Rivers	GSW and Cover 2020v100 watermask product	GA-LinkNet	When compared with GSW 19 (plus World Cover 2020), the OA was 0.959 (0.965) and 0.976 (0.981), the mIoU was 0.785 (0.817) and 0.641 (0.728), and the F1 scores were 0.879 (0.899) and 0.781 (0.843) for the Amazon and Congo regions, respectively. The results were in better agreement with the combined water masks whose water coverage was higher.
Bhattacharya et al. [147]	Spire Global, Sentinel-1, Sentinel-2	SNR	Louisiana and Mississippi	–	Threshold assignments	This study shows potential application of GNSS-R datasets along with optical and radar sensors to classify SPs over land and water to generate maps with water extent.
Liu et al. [125]	CYGNSS	ESR	Africa, East China, North America(1km)	GSW	An RF water mapping algorithm	An RF water mapping algorithm is developed with multiple statistical features as inputs. The presented algorithm outperforms the benchmark across the board.
Zhang et al. [148]; Scott et al. [149]	Spire Global, CYGNSS; Spire GNSS-R Grazing Angle Data	Residule carrier phase amd carrier phase hereafter, SNR; SNR	Lake Okeechobee	–	–	By comparing to the GSWE surface water boundaries, the disagreements of the GNSS-R ones based on Spire data are typically less than 0.73 km, with a mean of 0.28 km and a standard deviation of 0.24 km. As for CYGNSS, the differences are mainly less than 0.43 km, with a mean of 0.18 km and a standard deviation of 0.16 km; There is a positive relationship between the SNR and circular length parameters with the amount of water contained in the GNSS-R signal footprint.
Kossieris et al. [140]	CYGNSS	SNR	Amazon River, Congo River	–	Unsupervised ML algorithms	The Accuracy of the DBCAN algorithm is 90.3%, while Recall is 83.1% thanks to the lowest number of FN among the clustering algorithms. The Precision is 19.6%. Also, Recall is 79.2%.
Loria et al. [150]	GNSS-R data from simulations and the CYGNSS mission.	SNR	–	SAR images	–	Shape-based algorithms offer similar detection performance, with the Level-1 PR and entropy having the best performance. Another advantage of these algorithms over the DDM PMR is the lack of requirement for an accurate DDM power calibration, which is difficult to attain in practice.
Carreno-Luengo et al. [151]	CYGNSS, Raw IF CYGNSS	SNR	Over the Congo basin; a Surface Water and Ocean Topography (SWOT) cal/val site in the Amazon basin; the Pacaya-Samiria region; and the Pantanal wetlands	The Pekel surface water mask	A 2-D Boolean algorithm	We find that GPS signals are coherently reflected from surface water bodies despite the impact of the intervening biomass cover. Results show the capability to detect and image small water bodies under heavy vegetation i.e. 400 ton/ha.
Carreno-Luengo et al. [141], [152]	CYGNSS raw IF data	Refletivity; NBRCS, Γ, SNR	–	–	Full entropy Efull method	The threshold levels (one for each observable) at the optimum operating points of the ROC curves can be used for coherence detection and, thus, for inland water bodies tracking; Results show that the fast entropy Efast method provides a performance comparable to the full entropy Efull.
Chang et al. [153]	CYGNSS	SNR	Lake Victoria (0.01° × 0.01°)	–	DPSD method	The probability of detection (POD) was 90.6%, the false positive rate (FPR) reaches 8.5%, while the false negative rate (FNR) for pixels identified as water in GSW but not in CYGNSS accounts for only 0.9%.
Setti and Tabibi [154]	CYGNSS	reflectivity	Amazon River Basin	SWAF-HR's minimum and maximum inundation maps, Chapman product	CYGNSS-derived method	CYGNSS outperforms SWAF-HR and Chapman in recall, NPV, F1 Score, IoU, and MCC. With an NPV of 0.97, it accurately recognizes land grid cells during maximum inundation. The IoU of 0.52 indicates a 52% overlap with SWAF-HR in water cell detection. Compared to SWAF-HR, CYGNSS detects approximately 27% more water. Compared to Chapman, it shows a 56% increase at maximum extent and 19% at minimum extent.
Zhang et al. [155]	CYGNSS raw IF data	PR, DLR	Qinghai Lake	–	The space-borne GNSS-R PR method, and the spaceborne GNSS-R DLR method	The retrieval errors are all smaller than 0.7 km (the spatial resolution distance of high spatiotemporal resolution DDM), which satisfies the retrieval accuracy.
Pavur et al. [156]	CYGNSS, MODIS, Landsat	SNR	the contiguous United States between approximate latitudes of 24° N to 37° N	Landsat water mask, MODIS water mask	Confusion matrices and related statistics	The observation systems collectively classified 2.3% of the study area as inland water. Of the pixels classified as inland water, 14.2% were classified by all three observation systems. 30.6% were classified by at least two observation systems: 18.2% by Landsat and MODIS, 6.5% by Landsat and CYGNSS, and 5.9% by CYGNSS and MODIS. The remaining 55% of inland water pixels were classified by only one system: 29% by CYGNSS, 19.4% by Landsat, and 6.8% by MODIS.

[1] ESR: equivalent specific reflection, DLR: effective area delay distance.

CYGNSS data are complementary to existing observation platforms, and the cross validation of CYGNSS retrieved wetlands with multiple datasets and the fusion of multi-source RS data to obtain higher spatial and temporal resolution surface water monitoring results must be the focus of future research. Meanwhile, the focus should be on the dynamic RS of wetlands based on multisource spaceborne GNSS-R data to better monitor the dynamic changes of wetlands.

VIII. DETECTING FIRE DISTURBANCES IN FORESTS USING SPACEBORNE GNSS-R

In recent years, global climate change has significantly increased the incidence and severity of forest disturbance caused by fires, leading to significant changes in forest ecosystems and affecting the ability of forests to provide resources for human needs.

TABLE VIII
RETRIEVAL APPROACH AND ACCURACY OF CURRENTLY PUBLISHED SPACEBORNE GNSS-R WETLAND DETECTION STUDIES[1]

Source	Satellites (Data)	GNSS-R Observables	Spatial Coverage	Ancillary data	Reference Data	Retrieval Models (Methods)	Main Results
Nghiem et al. [157]	Aircraft data, TDS-1	Reflected power	Mississippi River and adjacent watersheds	QuikSCAT wet surface extent, MODIS, Landsat NDVI	–	–	Flooded wetlands can be identified under different vegetation conditions, including dense rice forests and dense tall tree forests. However, the capabilities provided by optical sensors and single station radars are limited
Jensen et al. [126]	CYGNSS	SNR, LES, TES	Peru's Ucayali-Marañon region of the Western Amazon	SAR Data	–	–	Ground measurements of high biomass and canopy covered areas confirmed that SAR did not identify submerged areas. The coordination of GNSS-R and L-band SAR has the potential for wider applications
Morris et al. [161]	CYGNSS	SNR	Everglades: a natural region of tropical wetlands in the southern portion of the U.S.A. state of Florida	GAP/LANDFIRE National Terrestrial Ecosystems 2011 dataset; EDEN water depth estimates	Pekel surface water dataset	Based on SNR threshold	The time sampling added by CYGNSS can supplement mature technologies that cannot capture dynamic wetland scenes. GNSS based technologies are less sensitive to vegetation and more sensitive to saturated soil, making them very useful in situations where other technologies are limited.
Rodriguez-Alvarez et al. [113]	CYGNSS	Reflectivity, peak SNR, TES, LES, width of the waveform, generalized linear observable	Pacaya-Samiria Natural Reserve, a tropical wetland complex located in the Peruvian Amazon	SRTM90 DEM; GFW biomass density (Mg/ha) map	PALSAR-2	MDTR	The accuracy of submerged vegetation areas is 69%, the accuracy of open water areas is 87%, and the accuracy of non submerged areas is 99%
Setti et al. [115]	CYGNSS	Effective surface reflectivity	Brazilian Pantanal	GPM precipitation data	Landsat GSWE seasonal water body product; SWAMPS wetland maps	Based on reflectivity threshold	The correlation between GNSS-R seasonal products and Landsat GSWE seasonal products is 0.74; The GNSS-R retrieval results have good consistency with the SWAMPS map (correlation of 0.88). Compared with SWAMPS, the total inundation range is usually overestimated, with an average overestimation rate of 19%.
Zeiger et al. [163]	CYGNSS	Reflectivity	Tropics	GlobBiomass AGB map; MODIS NDVI; SMAP SM;ESA CCI land cover maps	GIEMS surface water extent; JERS dual-season wetland classification; MODIS surface water; PALSAR flood maps; RFW dataset	Linear regression	Compared with the MODIS and GIEMS datasets at the regional scale, the RMSD of the CYGNSS method is 20% and the correlation is 0.60. CYGNSS displays a higher level of spatial detail than previously obtained through GIEMS.

[1]EDEN: everglades depth estimation network; MDTR: multiple decision tree randomized algorithm; PALSAR-2: phased-array L-band synthetic aperture radar; SRTM90: Shuttle Radar Topographic Mission 90 m resolution; GFW: global forest watch; GSWE: global surface water explorer; SWAMPS: surface water microwave product series, ESA: European Space Agency; CCI: climate change initiative; PALSAR: phased-array type L-band synthetic aperture radar; RFW: regularly flooded wetland; RMSD: root-mean-square deviation.

GNSS-R provides a new observation method for fire monitoring, which complements traditional fire monitoring methods by increasing the temporal and spatial coverage of burned areas. In 2021, Santi et al. [167] assessed the sensitivity of GNSS-R observations (SNR and equivalent reflectivity) to forest disturbances, developed an algorithm for identifying burned areas based on CYGNSS data, and validated it in the fire-affected equatorial African region of Angola using ten years of fire-affected data from ESA. CCI burned area maps were validated as reference data, confirming the potential of detecting fire-induced forest disturbances based on CYGNSS constellations. Despite the simplicity of the methodology, the proposed approach demonstrates the feasibility of using signals of opportunity for forest disturbance monitoring. To improve the detection algorithms, subsequently, classifiers based on SVM and RF have subsequently been implemented to distinguish burnt/unburned pixels in images. In addition, regressors based on ANN, RF, and support vector regression have been used to estimate the proportion of burnt areas within pixels [168]. This algorithm takes CYGNSS observations (i.e., SNR and equivalent reflection) as inputs and as auxiliary information for incidence angle and forest AGB. All algorithms are able to classify with an overall accuracy of over 98%, while for the change detection method that exhibits the worst performance (i.e., the best threshold detection combining SNR and equivalent reflection), the accuracy of identifying burn areas is about 40%. For all other methods, the accuracy is between 70% and 80%. The extremely imbalanced dataset has a percentage of burned pixels lower than 0.5% of the total dataset, which poses significant limitations for training. This may have affected the retrieval to some extent. These machine-learning algorithms demonstrate the feasibility and potential of using spaceborne GNSS-R technology for forest disturbance monitoring. Therefore, CYGNSS or other GNSS-R satellites can serve as valuable supplements to current and future missions to increase the time coverage of observations of burned areas. In order to expand the generalization ability of the proposed algorithm, auxiliary information such as topography and land cover should be taken into account, and their impact evaluated. Within this context, future research will focus on other areas with more complex topography [169].

IX. RETRIEVING LAND TOPOGRAPHY USING SPACEBORNE GNSS-R

Retrieval of topography parameters based on GNSS-R is also a new research topic. Carreno-Luengo et al. [170] found a functional relationship between the DDM of CYGNSS and several topography parameters of a digital elevation model (DEM). They used a target area in South Asia to observe the surface curvature. The results show that the trailing edge and albedo are closely related to the topographic humidity index. Meanwhile, Carreno-Luengo et al. [171] investigated the effect of rough topography on GNSS-R observations. The results show that the topography ruggedness index and profile curvature have a moderate to strong effect on the CYGNSS-derived trailing edge and low elevation reflectivity. Stilla et al. [172] used CYGNSS GNSS-R observations for the first time for characterizing the surface properties of the Sahara desert. It was shown that a strong correlation between roughness parameters and reflectivity can be used to characterize surface properties. By comparison with SAR measurements, reflectance is found to exhibit a robust correlation with roughness. An empirical relationship

between reflectance and roughness was established using ground measurements, and a map of four types of roughness in the Sahara was proposed. Further research is needed in the future on the interpretation of dune signals and validation with physical models. Dente et al. [173] presented an upgraded version of the soil and vegetation reflection simulator (SAVERS) simulator for modeling GNSS-R signals received by spaceborne sensors. The simulator estimates the SR signal from topographic data, considering parameters such as local elevation, slope and slope direction, as well as factors such as humidity, roughness, and vegetation properties. Through validation, it was found that topographic variations significantly affect the reflectivity, and the simulation results match the measured results. The simulator was also used for sensitivity analyses, and the results showed that SM was insensitive to topography, but biomass showed different saturation effects in different topographies. Therefore, it is recommended that the SM and biomass retrieval algorithms should consider the effects of topography and that the design of the spaceborne GNSS-R instrument should take into account the characteristics of signal reception in mountainous areas. Song et al. [174] explored the effect of topography on spatial GNSS-R geometry computation and proposed a new strategy for geometry computation. The strategy is based on the unique properties of ellipsoids, which, together with a fast empirical model, significantly improves the computational efficiency. The methodology is validated by a single trajectory study of the South West Greenland ice surface, which shows that neglecting slope and orientation leads to significant theoretical point errors. The study also points out the possible errors associated with large-scale slopes and the impact that extreme topographic slopes of the ocean may have on high-precision carrier-phase altimetry under grazing angle conditions, which need to be further considered in future precision altimetry studies. Later, Campbell et al. [175] developed a model to describe the effect of topography on DDMs. Wang and Morton [176] used GNSS-R for land surface altimetry applications. They processed CYGNSS raw IF data using adaptive hybrid tracking. They also studied semicoherent land reflection events over Vietnam and coherent reflections over the Orinoco River, and the results demonstrated pseudorange-based land altimetry accuracy to the meter level and inland water body surface height retrieval accuracy to the centimeter level. The current study demonstrates the feasibility of spaceborne GNSS-R land topography retrieval; however, there are relatively few related studies that are in the exploratory stage and there is much room for future development.

X. Some Further Applications

In addition to the hot topics of research on spaceborne GNSS-R land applications reviewed in the previous sections, some compelling emerging applications are also of great value for scientific research, such as retrieval of inland water surface heights [159], [177], [178], [179], river slopes [180], [181], and river widths [182], [183], monitoring of lake ice [184], estimation of wind and wave heights over inland waters [185], [186], and monitoring of reservoir water levels [187]. In 2018, Li et al. [159] demonstrated the feasibility and performance of the carrier phase-delay altimetry method for lake altimetry with the CYGNSS Raw IF dataset collected on Qinghai Lake. Zhang and Morton [177] estimated the water levels of five lakes [Salton Sea (33.3° N, 115.7° W), Lake Okeechobee (26.9° N, 80.9° W), Tonle Sap Lake (12.8° N, 104.1° E), Kainji Lake (10.2° N, 4.5° E), and Lake Guri (7.3° N, 62.9° W)] using the coherent reflectance-dominated DDM for the years 2020 to 2022. Compared with the radar altimetry observation results, the overall deviation of CYGNSS results is about 2.0 m, the root-mean-square difference is about 3.1 m, and the unbiased root mean square difference (ubRMSD) is about 2.4 m. This study demonstrates the feasibility of spaceborne GNSS-R for measuring inland water levels. Existing work also highlights the need for dual-frequency receivers to correct for ionospheric effects to achieve highly accurate altimetry. In 2022, Wang and Morton used the CYGNSS Raw IF dataset to estimate river slopes, and the results demonstrated the potential of CYGNSS to provide high temporal and spatial resolution observations of river slopes [181]. In 2023, Zhang et al. [155] also used CYGNSS Raw IF data to study lake boundary detection for the Qinghai Lake area in 2018, and compared the retrieval detection results with the Google Earth topography distribution results; the retrieval results had an error of about 0.5 km, which proved that the CYGNSS Raw IF data have good application prospects in lake boundary detection. Warnock and Ruf [182] analyzed the response of different flow sections of the Pascagoula River using spaceborne GNSS-R raw IF signals and deduced the signal widths by analyzing the widths of the peak signals from the center of the river to either side of the peak. The results show that the associated GNSS-R width of the river is highly correlated with the observed flow and that there is an approximately monotonic relationship between the two. This demonstrates the potential of GNSS-R-based methods as a means of estimating river flow and width, providing important inputs to remotely sensed flow retrieval algorithms. However, further research on a wider range of datasets is needed to validate the robustness of the method and the limitations of its applicability. More recently, Warnock et al. [183] described the use of CYGNSS to measure uncertainty in river widths to advance research on GNSS-R as a characterization of inland water bodies. The accuracy of the forward model was demonstrated by comparing the simulated data with the actual observations, and the relationship between river width and the measured peak SNR was analyzed. The results indicate that in simple river scenarios, GNSS-R raw IF signal data can measure rivers with a width of 160–192 m, with an error of about 3%. In addition, simulation analysis was conducted on the lake clutter near the river, and it was found that about 500 m is the range where the lake has a significant impact on the SNR of the river. Overall, the study presents a robust modeling approach to estimate river widths within an uncertainty of approximately 5 m. However, further research is required to determine the limitations of retrieving river widths from GNSS-R data and the effects of unconsidered factors. In 2023, Ghiasi et al. [184] used CYGNSS GNSS-R to monitor lake ice phenology for the first time on Qinghai Lake on the Tibetan Plateau. By analyzing GNSS-R SNR data from four ice seasons, it was possible to detect the formation and melting

of lake ice. The results of the study are consistent with the MODIS image record and validate the capability of GNSS-R for lake ice phenology monitoring. The study also revealed the sensitivity of GNSS-R to lake melting, explaining the discrepancy between GNSS signals and open water conditions determined by MODIS. This study demonstrates the potential of GNSS-R as a platform for monitoring lake ice phenology and suggests plans for further research, including observations of other lakes and the use of methods such as ML to improve the monitoring of lake conditions. In addition, it is expected that the use of spaceborne GNSS-R technology to monitor lake ice thickness in the future is also very promising; although there is no literature report so far, it is also a hot topic worth paying attention to. Surface wind speed and wave height measurements of inland water bodies using spaceborne GNSS-R have also attracted the attention of some scholars. GNSS-R utilizes the scattering properties of coherent signals to measure the surface roughness of inland water bodies, especially the height of waves caused by wind. The method can be used in conjunction with wind-wave modeling to retrieve wind vectors and wave heights in inland water bodies and has a wide range of scientific applications, including studies of nearshore ecosystems, climate change impacts on inland water bodies, sediment resuspension, biomass production, and fish habitats. The results show that the coherent signal is highly sensitive to changes in water surface roughness and can predict wave height changes for different wind speeds and directions. The method of retrieving wind speed was validated using data recorded by CYGNSS satellites and good results were obtained [185]. However, for inland water bodies with vegetation, the vegetation will influence the surface roughness and further research is needed. At present, by combining technologies such as passive GNSS-R, active SAR, and radar sensors, it is possible to detect and characterize the wind speed of small and medium-sized inland water bodies, providing high spatial and temporal resolution wind speed data. These techniques can use features such as water surface roughness and dielectric properties to estimate wind speed and provide reliable results under different weather conditions and cloud cover. However, further refinement and validation of the feasibility of these methods is still required for inland water bodies smaller than 100 km^2 [186], [188]. Past studies have demonstrated the feasibility of using measurements from the NASA CYGNSS mission to map inland water bodies. However, challenges remain in monitoring the dynamic characteristics of water bodies, such as reservoir storage levels. To this end, Brendle et al. [187] explored alternative sensing methods based on the CYGNSS Level-1 product, which allows for a finer estimation of reservoir storage levels. By using data from three example reservoirs for analysis, it was found that the detected water level is related to the RMSE of the relative water level, with an error range of 8%–20%, depending on the complexity of the observation scenario. The preliminary results demonstrate the potential of the spaceborne GNSS-R system in reservoir water level monitoring, with a correlation of approximately 86% with onsite data. It is worth noting that the innovative application of using spaceborne GNSS-R technology to monitor drought has also been reported in recent works [189], [190]. In addition, utilizing spaceborne GNSS-R RS of algal blooms has become an interesting topic [191], [192]. Lake algal blooms have become a serious environmental problem caused by the excessive growth of plankton in many water bodies, but current relevant personnel have not paid enough attention. Further attention and research are still needed in the future. It is worth mentioning that although spaceborne GNSS-R is widely used for surface hydrological monitoring, the research on the spatiotemporal response mechanism of GNSS reflection signals to precipitation is still of limited attention [193], which will also be an interesting topic in future research.

In 2023, Wang [194], [195] used Grazing-angle GNSS-R for the first time to determine the tropospheric delay and water vapor content by estimating the tropospheric delay using the dual-frequency GPS signals collected by Grazing-angle from sea-ice, ocean reflections, and compared it with the Sentinel-3 Ocean and Land Color Instrument measurements (OLCI) and ERA5 products, and showed that the GNSS-R method is in good agreement with Sentinel-3 OLCI and ERA5. This technique has good potential to complement existing methods and provide high-precision and high-resolution observations of tropospheric water vapor in open water and ice where water vapor measurements are often difficult to obtain. Large inland waters tend to be more prone to GNSS-R coherent signals; therefore, the author can infer that the use of spaceborne GNSS-R techniques for integrated water vapor retrieval over inland waters is expected to be very promising, and needs to be further analyzed and quantified.

GNSS-R has great potential for integration with other RS data sources and ML technologies [196]. Integrating GNSS-R with other RS data and ML technologies can provide complementary data sources, multidimensional information fusion, improve spatial resolution, enhance prediction and early warning capabilities, and achieve real-time monitoring and decision support. This integrated method will become a focus of future research and application, providing more comprehensive, accurate, and timely information support for environmental monitoring, resource management, and disaster monitoring.

XI. Discussion and Summary

A. Discussion

Small and inexpensive spaceborne GNSS-R satellites, such as the CYGNSS, can be used for land RS because they offer many benefits, including providing daily and daily-independent weather measurements. However, these satellites have several limitations. Compared with conventional RS satellites, the positions of GNSS transmitters and GNSS-R satellites are constantly changing, leading to chaotic and random observations from the Earth's surface. In addition, these observations have different spatial resolutions (depending on several factors such as terrain and roughness) and revisit times. In addition, dense vegetation can reduce the performance of these observations [43]. A prominent drawback of CYGNSS is that it only scans the area with an inclination between 38° N and 38° since this mission was initially designed to monitor ocean and wind in the inner core of tropical cyclones.

Traditional radiometers typically provide lower time resolution (two to three days) and are not sensitive to surface roughness. However, these measurements are highly sensitive to surface brightness and RFI. At present, the measurements provided by the SMOS of the ESA and the SMAP of the NASA are the main sources of large-scale SM monitoring or soil freeze-thaw monitoring, with a spatial resolution of ∼40 km and a temporal resolution of two to three days [27]. In publications, authors often take the average of GNSS-R (e.g., CYGNSS) observation results on predefined 36 or 25 km grids for these tasks to match them, thereby disrupting the inherent high spatial sampling resolution of GNSS-R measurements. Compared to the two, spaceborne GNSS-R can provide high spatial and temporal resolution measurements.

Compared with other RS technologies (e.g., SAR and multispectral (MS) RS), spaceborne GNSS-R has not yet reached sufficient maturity in most land applications. Many research works still focus on analyzing the sensitivity of GNSS-R signals to geophysical parameters of interest (e.g., vegetation parameters, soil freeze-thaw state, and precipitation). The feasibility of using spaceborne GNSS-R for some applications has not been fully evaluated. Therefore, the current research work is still limited to quantitative analysis. Optical and thermal infrared RS are limited by weather conditions and cannot work around the clock. Microwave RS has overcome these limitations. Due to its long wavelength, it has certain penetrability to rain clouds and can operate under all weather conditions. L-band satellites such as Japanese Earth Resources Satellite-1 (JERS-1), Advanced Land Observing Satellite (ALOS), and ALOS-2 can be used for vegetation monitoring, but their six-week time resolution still limits their practical scientific applications. Due to the fact that spaceborne GNSS-R is essentially a bistatic/multistatic radar operating in the L-band, the significant advantage of using this method to observe vegetation parameters compared to traditional single base radar is that the signal response to biomass is not as easily saturated as single base radar. Therefore, using this RS method to monitor vegetation parameters has advantages that traditional RS methods cannot match. However, observing geometric changes is one of the potential drawbacks of spaceborne GNSS-R. Therefore, how to use the scattering characteristics under different observation geometries and polarization conditions to determine the optimal observation combination (observation geometry and polarization), and develop quantitative retrieval methods will be a focus of future research [28].

Other sources of uncertainty in the retrieval of land surface geophysical parameters (such as SM and forest biomass, etc.) by spaceborne GNSS-R may be related to calibration issues (such as unknown changes in transmission power and antenna gain characteristics), which have not been fully resolved in the current mission [191]. It is necessary to mitigate these fluctuations in order to achieve reasonable retrieval performance of the target quantity. Therefore, appropriate calibration, noise mitigation, and spatial and temporal aggregation strategies must be implemented to optimize the final resolution of the product. The existing work also solves the problem of requiring auxiliary data to retrieve target parameters to compensate for the influence of other features that affect the signal, including small-scale surface roughness and terrain (which is common in RS). The dual polarization GNSS-R observation has been proven to be very useful on low platforms but has not yet been tested on satellites, except for experiments using SMAP radar as a GNSS receiver [197], [198], [199], [200]. The polarization application of spaceborne GNSS-R has not yet been used in areas with cryosphere and dense vegetation. The integration of all types of GNSS constellations with new polarization schemes and higher bandwidth signals will allow for better retrieval to estimate several highly relevant land surface geophysical parameters, such as inland water bodies, SM, wetlands, lakes, and vegetation [201].

Compared with other RS technologies, spaceborne GNSS-R has certain advantages and characteristics in terms of the data acquisition cost, spatiotemporal resolution, measurement parameters, and applications, as well as data processing and interpretation. However, different RS technologies may be more applicable in specific application scenarios, so it is important to comprehensively consider the advantages and disadvantages of various technologies and choose appropriate RS technologies for analysis and application. Compared to spaceborne GNSS-R, SAR and MS RS can provide higher spatial resolution, typically at the meter level. For retrieval problems with alternative solutions (such as SM using microwave radiometers such as SMOS, Aquarius, and SMAP, soil freeze-thaw monitoring using SMAP or SMOS microwave radiometers, inland water detection using the GFM data derived from Sentinel-1 radar imaging, SWAMPS, global surface water (GSW), and global surface water dynamics), it is worth considering how these systems benefit from each other, that is, how they complement each other.

B. Summary

This article provides a comprehensive review of the application research progress in the field of spaceborne GNSS-R land RS, including the current development status of spaceborne GNSS-R constellations and land application fields, SM and soil salinity retrieval, vegetation monitoring, soil F/T, flood detection, inland water bodies, wetland dynamics, forest fire disturbance detection, land topography measurement, and future innovative application directions. In addition, this article also provides an overview, advantages, and future application prospects of China's first TM-1 GNSS-R constellation that is compatible with four navigation systems: BeiDou, GPS, GLONASS, and Galileo.

In recent years, spaceborne GNSS-R as an emerging RS technology has made remarkable progress in the field of land RS. However, in order to be comparable to conventional RS techniques, more advanced spaceborne GNSS-R modeling algorithms for different applications need to be developed in the future or combined with other techniques to obtain improved products. At the same time, conducting ground-based and airborne experiments to improve basic theories and models (such as electromagnetic scattering models for L-band signals), developing

optimized designs for the next generation of spaceborne GNSS-R instruments, and conducting in-orbit experiments to achieve multifrequency/multisystem, multipolarization, and multiobservation modes, thereby improving observation performance in terms of accuracy, accuracy, and spatiotemporal resolution. In addition, the current research on land RS applications is focused on using GNSS-R data from CYGNSS/TDS-1/Spire satellite missions. In the future, advanced modeling algorithms and new products can be developed by comprehensively utilizing other multisource spaceborne GNSS-R (such as FY-3E/3F/3G, BF-1 A/B, TM-1, and HydroGNSS) missions and multisystem GNSS (such as BeiDou, GPS, GLONASS, Galileo, QZSS) reflection signals. Combining with the needs of land RS applications, more valuable information and insights can be provided for environmental research, resource management, and natural disaster monitoring by developing advanced modeling algorithms and new products. In addition, innovative application directions should be the focus of research to explore the potential of spaceborne GNSS-R in new areas.

ACKNOWLEDGMENT

The authors would like to thank the anonymous reviewers for their in-depth reviews and helpful suggestions that have largely contributed to improving this article. TM-1 satellite constellation GNSS-R data are sourced from Aerospace Tianmu (Chongqing) Satellite Science and Technology Co., Ltd. and Aerospace Science and Industry (Beijing) Spatial Information Application Co., Ltd. We are also very grateful to them for providing TM-1 GNSS-R data for free.

REFERENCES

[1] C. D. Hall and R. A. Cordey, "Multistatic scatterometry," in *Proc. Int. Geosci. Remote Sens. Symp., 'Remote Sens.: Moving Toward 21st Century'*, 1988, vol. 1, pp. 561–562.

[2] M. Martin-Neira, "A passive reflectometry and interferometry system (PARIS): Application to ocean altimetry," *ESA J.*, vol. 17, pp. 331–355, 1993.

[3] M. Unwin, S. Gleason, and M. Brennan, "The space GPS reflectometry experiment on the U.K. disaster monitoring constellation satellite," in *Proc. 16th Int. Tech. Meeting Satell. Division Inst. Navigation*, 2003, pp. 2656–2663.

[4] M. Unwin, P. Jales, J. Tye, C. Gommenginger, G. Foti, and J. Rosello, "Spaceborne GNSS-reflectometry on TechDemoSat-1: Early mission operations and exploitation," *IEEE J. Sel. Topics Appl. Earth Observ. Remote Sens.*, vol. 9, no. 10, pp. 4525–4539, Oct. 2016.

[5] J. Tye, P. Jales, M. Unwin, and C. Underwood, "The first application of stare processing to retrieve mean square slope using the SGR-ReSI GNSS-R experiment on TDS-1," *IEEE J. Sel. Topics Appl. Earth Observ. Remote Sens.*, vol. 9, no. 10, pp. 4669–4677, Oct. 2016.

[6] C. Ruf et al., *CYGNSS Handbook Cyclone Global Navigation Satellite System: Deriving Surface Wind Speeds in Tropical Cyclones*. Ann Arbor, MI, USA: National Aeronautics and Space Administration, 2016, p. 154.

[7] C. Ruf et al., "CYGNSS: Enabling the future of hurricane prediction [remote sensing satellites]," *IEEE Geosci. Remote Sens. Mag.*, vol. 1, no. 2, pp. 52–67, Jun. 2013.

[8] M. P. Clarizia and C. S. Ruf, "Wind speed retrieval algorithm for the cyclone global navigation satellite system (CYGNSS) mission," *IEEE Trans. Geosci. Remote Sens.*, vol. 54, no. 8, pp. 4419–4432, Aug. 2016.

[9] H. Carreno-Luengo et al., "3Cat-2—An experimental nanosatellite for GNSS-R earth observation: Mission concept and analysis," *IEEE J. Sel. Topics Appl. Earth Observ. Remote Sens.*, vol. 9, no. 10, pp. 4540–4551, Oct. 2016.

[10] A. Camps et al., "FSSCAT, the 2017 Copernicus masters' 'ESA sentinel small satellite challenge' winner: A federated polar and soil moisture tandem mission based on 6U CubeSats," in *Proc. IEEE Int. Geosci. Remote Sens. Symp.*, 2018, pp. 8285–8287.

[11] D. Masters, "Design and planning for the first spire GNSS-R missions of 2019," in *Proc. IEEE GRSS, GRSS, Spec. Meeting Reflectometry Using GNSS Other Signals Opportunity*, 2019.

[12] D. Masters et al., "Status and plans for Spire's growing commercial constellation of GNSS science CubeSats," in *Proc. Joint 6th ROM SAF User Workshop 7th IROWG Workshop*, 2019, pp. 19–25.

[13] P. T. Setti Jr and S. Tabibi, "Evaluation of spire GNSS-R reflectivity from multiple GNSS constellations for soil moisture estimation," *Int. J. Remote Sens.*, vol. 44, no. 20, pp. 6422–6441, 2023.

[14] C. Jing, X. Niu, C. Duan, F. Lu, G. Di, and X. Yang, "Sea surface wind speed retrieval from the first Chinese GNSS-R mission: Technique and preliminary results," *Remote Sens.*, vol. 11, no. 24, 2019, Art. no. 3013.

[15] C. Jing et al., "A review of the BuFeng-1 GNSS-R mission: Calibration and validation results of sea surface and land surface," *Geo-Spatial Inf. Sci.*, pp. 1–15, 2024, doi: 10.1080/10095020.2024.2330547.

[16] W. Wan et al., "Initial evaluation of the first Chinese GNSS-R mission BuFeng-1 A/B for soil moisture estimation," *IEEE Geosci. Remote Sens. Lett.*, vol. 19, 2022, Art. no. 8017305.

[17] Y. Sun et al., "The status and progress of Fengyun-3E GNOS II mission for GNSS remote sensing," in *Proc. IEEE Int. Geosci. Remote Sens. Symp.*, 2019, pp. 5181–5184.

[18] National Satellite Meteorological Center, 2023. [Online]. Available: http://www.nsmc.org.cn/nsmc/cn/instrument/GNOS-2.html

[19] National Satellite Meteorological Center, 2023. [Online]. Available: https://satellite.nsmc.org.cn/FY3G/html/IOTDATASET.html

[20] P. Zhang et al., "FY-3E: The first operational meteorological satellite mission in an early morning orbit," *Adv. Atmospheric Sci.*, vol. 39, no. 1, pp. 1–8, 2022.

[21] A. Dielacher et al., "The ESA passive reflectometry and dosimetry (PRETTY) mission," in *Proc. IEEE Int. Geosci. Remote Sens. Symp.*, 2019, pp. 5173–5176.

[22] M. J. Unwin et al., "An introduction to the HydroGNSS GNSS reflectometry remote sensing mission," *IEEE J. Sel. Topics Appl. Earth Observ. Remote Sens.*, vol. 14, pp. 6987–6999, 2021.

[23] S. Jin, G. P. Feng, and S. Gleason, "Remote sensing using GNSS signals: Current status and future directions," *Adv. Space Res.*, vol. 47, no. 10, pp. 1645–1653, 2011.

[24] S. Jin and A. Komjathy, "GNSS reflectometry and remote sensing: New objectives and results," *Adv. Space Res.*, vol. 46, no. 2, pp. 111–117, 2010.

[25] A. Camps et al., "Land monitoring using GNSS-R techniques: A review of recent advances," in *Proc. IEEE Int. Geosci. Remote Sens. Symp.*, 2013, pp. 4026–4029.

[26] K. Yu, C. Rizos, D. Burrage, A. G. Dempster, K. Zhang, and M. Markgraf, "An overview of GNSS remote sensing," *EURASIP J. Adv. Signal Process.*, vol. 2014, pp. 1–14, 2014.

[27] X. Wu, W. Ma, J. Xia, W. Bai, S. Jin, and A. Calabia, "Spaceborne GNSS-R soil moisture retrieval: Status, development opportunities, and challenges," *Remote Sens.*, vol. 13, no. 1, 2020, Art. no. 45.

[28] X. Wu, P. Guo, Y. Sun, H. Liang, X. Zhang, and W. Bai, "Recent progress on vegetation remote sensing using spaceborne GNSS-reflectometry," *Remote Sens.*, vol. 13, no. 21, 2021, Art. no. 4244.

[29] H. Carreno-Luengo et al., "The IEEE-SA working group on spaceborne GNSS-R: Scene study," *IEEE Access*, vol. 9, pp. 89906–89933, 2021.

[30] N. Pierdicca et al., "The potential of spaceborne GNSS reflectometry for soil moisture, biomass, and freeze–thaw monitoring: Summary of a European Space Agency-funded study," *IEEE Geosci. Remote Sens. Mag.*, vol. 10, no. 2, pp. 8–38, Jun. 2022.

[31] N. Rodriguez-Alvarez, J. F. Munoz-Martin, and M. Morris, "Latest advances in the global navigation satellite system–reflectometry (GNSS-R) field," *Remote Sens.*, vol. 15, no. 8, 2023, Art. no. 2157.

[32] C. Yang, K. Mao, Z. Guo, J. Shi, S. M. Bateni, and Z. Yuan, "Review of GNSS-R technology for soil moisture inversion," *Remote Sens.*, vol. 16, no. 7, 2024, Art. no. 1193.

[33] S. Gleason et al., "Detection and processing of bistatically reflected GPS signals from low earth orbit for the purpose of ocean remote sensing," *IEEE Trans. Geosci. Remote Sens.*, vol. 43, no. 6, pp. 1229–1241, Jun. 2005.

[34] H. Carreno-Luengo, S. Lowe, C. Zuffada, S. Esterhuizen, and S. Oveisgharan, "Spaceborne GNSS-R from the SMAP mission: First assessment of polarimetric scatterometry over land and cryosphere," *Remote Sens.*, vol. 9, no. 4, 2017, Art. no. 362.

[35] J. F. Munoz-Martin et al., "3Cat-4: Combined GNSS-R, L-Band radiometer with RFI mitigation, and AIS receiver for a I-Unit CubeSat based on software defined radio," in *Proc. IEEE Int. Geosci. Remote Sens. Symp.*, 2018, pp. 1063–1066.

[36] NanoSat Lab, 2024. [Online]. Available: https://nanosatlab.upc.edu/en/missions-and-projects/3cat-4

[37] J.-C. Juang, S.-H. Ma, and C.-T. Lin, "Study of GNSS-R techniques for FORMOSAT mission," *IEEE J. Sel. Topics Appl. Earth Observ. Remote Sens.*, vol. 9, no. 10, pp. 4582–4592, Oct. 2016.

[38] H. Y. Wang and J. C. Juang, "Retrieval of ocean surface wind speed using reflected BPSK/BOC signals," *Remote Sens.*, vol. 12, no. 17, 2020, Art. no. 2698.

[39] M. Unwin, J. Rawlinson, L. King, G. Foti, M. Hammond, and T. Burger, "GNSS-reflectometry activities on the DoT-1 microsatellite in preparation for the hydroGNSS mission," in *Proc. IEEE Int. Geosci. Remote Sens. Symp.*, 2021, pp. 1288–1290.

[40] N. Fu and F. Li, "An introduction of GNSS reflectometer remote sensing mission from Yunyao Aerospace Technology Co., Ltd," in *Proc. IEEE Spec. Meeting Reflectometry Using GNSS Other Signals Opportunity*, 2021, pp. 77–81.

[41] Y. Sun et al., "GNOS-II on fengyun-3 satellite series: Exploration of multi-GNSS reflection signals for operational applications," *Remote Sens.*, vol. 15, no. 24, 2023, Art. no. 5756.

[42] N. Rodriguez-Alvarez et al., "Soil moisture retrieval using GNSS-R techniques: Experimental results over a bare soil field," *IEEE Trans. Geosci. Remote Sens.*, vol. 47, no. 11, pp. 3616–3624, Nov. 2009.

[43] A. Camps et al., "Sensitivity of GNSS-R spaceborne observations to soil moisture and vegetation," *IEEE J. Sel. Topics Appl. Earth Observ. Remote Sens.*, vol. 9, no. 10, pp. 4730–4742, Oct. 2016.

[44] C. Chew, R. Shah, C. Zuffada, G. Hajj, D. Masters, and A. J. Mannucci, "Demonstrating soil moisture remote sensing with observations from the U.K. TechDemoSat-1 satellite mission," *Geophysical Res. Lett.*, vol. 43, no. 7, pp. 3317–3324, 2016.

[45] H. Kim and V. Lakshmi, "Use of cyclone global navigation satellite system (CyGNSS) observations for estimation of soil moisture," *Geophysical Res. Lett.*, vol. 45, no. 16, pp. 8272–8282, 2018.

[46] C. C. Chew and E. E. Small, "Soil moisture sensing using spaceborne GNSS reflections: Comparison of CYGNSS reflectivity to SMAP soil moisture," *Geophysical Res. Lett.*, vol. 45, no. 9, pp. 4049–4057, 2018, doi: 10.1029/2018GL077905.

[47] G. Yang et al., "An illustration of FY-3E GNOS-R for global soil moisture monitoring," *Sensors (Basel)*, vol. 23, no. 13, Jun. 2023, Art. no. 5825.

[48] W. Ban, K. Yu, and X. Zhang, "GEO-satellite-based reflectometry for soil moisture estimation: Signal modeling and algorithm development," *IEEE Trans. Geosci. Remote Sens.*, vol. 56, no. 3, pp. 1829–1838, Mar. 2018.

[49] O. Eroglu, M. Kurum, D. Boyd, and A. C. Gurbuz, "High spatio-temporal resolution CYGNSS soil moisture estimates using artificial neural networks," *Remote Sens.*, vol. 11, no. 19, 2019, Art. no. 2272.

[50] Y. Jia et al., "GNSS-R soil moisture retrieval based on a XGboost machine learning aided method: Performance and validation," *Remote Sens.*, vol. 11, no. 14, 2019, Art. no. 1655.

[51] Y. Jia, S. Jin, P. Savi, Q. Yan, and W. Li, "Modeling and theoretical analysis of GNSS-R soil moisture retrieval based on the random forest and support vector machine learning approach," *Remote Sens.*, vol. 12, no. 22, 2020, Art. no. 3679.

[52] Q. Yan, W. Huang, S. Jin, and Y. Jia, "Pan-tropical soil moisture mapping based on a three-layer model from CYGNSS GNSS-R data," *Remote Sens. Environ.*, vol. 247, 2020, Art. no. 111944.

[53] V. Senyurek, F. Lei, D. Boyd, M. Kurum, A. C. Gurbuz, and R. Moorhead, "Machine learning-based CYGNSS soil moisture estimates over ISMN sites in CONUS," *Remote Sens.*, vol. 12, no. 7, 2020, Art. no. 1168.

[54] E. Santi et al., "Combining CyGNSS and machine learning for soil moisture and forest biomass retrieval in view of the ESA scout hydroGNSS mission," in *Proc. IEEE Int. Geosci. Remote Sens. Symp.*, 2022, pp. 7433–7436.

[55] T. M. Roberts, I. Colwell, C. Chew, S. Lowe, and R. Shah, "A deep-learning approach to soil moisture estimation with GNSS-R," *Remote Sens.*, vol. 14, no. 14, 2022, Art. no. 3299.

[56] M. M. Nabi, V. Senyurek, F. Lei, M. Kurum, and A. C. Gurbuz, "Quasi-global assessment of deep learning-based CYGNSS soil moisture retrieval," *IEEE J. Sel. Topics Appl. Earth Observ. Remote Sens.*, vol. 16, pp. 5629–5644, 2023.

[57] Q. Hu et al., "Research on soil moisture inversion method for canal slope of the middle route project of the south to north water transfer based on GNSS-R and deep learning," *Remote Sens.*, vol. 15, no. 17, 2023, Art. no. 4340.

[58] W. Yang, F. Guo, X. Zhang, and Y. Zhu, "An improved method for water body removal in spaceborne GNSS-R soil moisture retrieval," *IEEE Trans. Geosci. Remote Sens.*, vol. 61, 2023, Art. no. 4701308.

[59] Q. Wang, J. Sun, X. Chang, T. Jin, J. Shang, and Z. Liu, "The correction method of water and fresnel reflection coefficient for soil moisture retrieved by CYGNSS," *Remote Sens.*, vol. 15, no. 12, 2023, Art. no. 3000.

[60] M. P. Clarizia, N. Pierdicca, F. Costantini, and N. Floury, "Analysis of CYGNSS data for soil moisture retrieval," *IEEE J. Sel. Topics Appl. Earth Observ. Remote Sens.*, vol. 12, no. 7, pp. 2227–2235, Jul. 2019.

[61] S. H. Yueh, R. Shah, M. J. Chaubell, A. Hayashi, X. Xu, and A. Colliander, "A semiempirical modeling of soil moisture, vegetation, and surface roughness impact on CYGNSS reflectometry data," *IEEE Trans. Geosci. Remote Sens.*, vol. 60, 2022, Art. no. 5800117.

[62] C. Yin et al., "Soil moisture retrieval from multi-GNSS reflectometry on FY-3E GNOS-II by land cover classification," *Remote Sens.*, vol. 15, no. 4, 2023, Art. no. 1097.

[63] M. M. Al-Khaldi, J. T. Johnson, A. J. O'Brien, A. Balenzano, and F. Mattia, "Time-series retrieval of soil moisture using CYGNSS," *IEEE Trans. Geosci. Remote Sens.*, vol. 57, no. 7, pp. 4322–4331, Jul. 2019.

[64] J. F. Munoz-Martin, D. Llaveria, C. Herbert, M. Pablos, H. Park, and A. Camps, "Soil moisture estimation synergy using GNSS-R and L-band microwave radiometry data from FSSCat/FMPL-2," *Remote Sens.*, vol. 13, no. 5, 2021, Art. no. 994.

[65] E. Santi et al., "Soil moisture and forest biomass retrieval on a global scale by using CyGNSS data and artificial neural networks," in *Proc. IEEE Int. Geosci. Remote Sens. Symp.*, 2020, pp. 5905–5908.

[66] Y. Jia et al., "Temporal-spatial soil moisture estimation from CYGNSS using machine learning regression with a pre-classification approach," *IEEE J. Sel. Topics Appl. Earth Observ. Remote Sens.*, vol. 14, pp. 4879–4893, 2021.

[67] Y. Jia, S. Jin, Q. Yan, P. Savi, R. Zhang, and W. Li, "An effective land type labeling approach for independently exploiting high-resolution soil moisture products based on CYGNSS data," *IEEE J. Sel. Topics Appl. Earth Observ. Remote Sens.*, vol. 15, pp. 4234–4247, 2022.

[68] V. Senyurek, F. Lei, D. Boyd, A. C. Gurbuz, M. Kurum, and R. Moorhead, "Evaluations of machine learning-based CYGNSS soil moisture estimates against SMAP observations," *Remote Sens.*, vol. 12, no. 21, 2020, Art. no. 3503.

[69] F. Lei et al., "Quasi-global machine learning-based soil moisture estimates at high spatio-temporal scales using CYGNSS and SMAP observations," *Remote Sens. Environ.*, vol. 276, 2022, Art. no. 113041.

[70] Y. Zhu, F. Guo, and X. Zhang, "Effect of surface temperature on soil moisture retrieval using CYGNSS," *Int. J. Appl. Earth Observation Geoinformation*, vol. 112, 2022, Art. no. 102929.

[71] S. Zhang et al., "Improvement of CYGNSS soil moisture retrieval model considering water and surface temperature," *Adv. Space Res.*, vol. 72, no. 8, pp. 3048–3064, 2023.

[72] T. Yang, W. Wan, Z. Sun, B. Liu, S. Li, and X. Chen, "Comprehensive evaluation of using TechDemoSat-1 and CYGNSS data to estimate soil moisture over Mainland China," *Remote Sens.*, vol. 12, 2020, Art. no. 1699.

[73] X. Wu, J. Xia, S. Jin, W. Bai, and Z. Dong, "Is soil salinity detectable by GNSS-R/IR?," in *Proc. IEEE Int. Geosci. Remote Sens. Symp.*, 2019, pp. 6227–6230.

[74] E. Loria, A. O'Brien, V. Zavorotny, B. Downs, and C. Zuffada, "Analysis of scattering characteristics from inland bodies of water observed by CYGNSS," *Remote Sens. Environ.*, vol. 245, 2020, Art. no. 111825.

[75] C. Chew and E. Small, "Description of the UCAR/CU soil moisture product," *Remote Sens.*, vol. 12, no. 10, 2020, Art. no. 1558.

[76] W. Li, E. Cardellach, F. Fabra, S. Ribó, and A. Rius, "Assessment of spaceborne GNSS-R ocean altimetry performance using CYGNSS mission raw data," *IEEE Trans. Geosci. Remote Sens.*, vol. 58, no. 1, pp. 238–250, Jan. 2020.

[77] C. S. Ruf et al., "The CYGNSS nanosatellite constellation hurricane mission," in *Proc. IEEE Int. Geosci. Remote Sens. Symp.*, 2012, pp. 214–216.

[78] J. F. Munoz-Martin and A. Camps, "Sea surface salinity and wind speed retrievals using GNSS-R and L-band microwave radiometry data from FMPL-2 onboard the FSSCat mission," *Remote Sens.*, vol. 13, no. 16, 2021, Art. no. 3224.

[79] C. Chew, J. T. Reager, and E. Small, "CYGNSS data map flood inundation during the 2017 Atlantic hurricane season," *Sci. Rep.*, vol. 8, no. 1, 2018, Art. no. 9336.

[80] J. Wang et al., "A remote sensing method for retrieving soil salinity based on CYGNSS data: Taking Yellow River Delta as an example," *Nat. Remote Sens. Bull.*, vol. 27, no. 2, pp. 351–362, 2023.

[81] J. Wang et al., "A novel retrieval model for soil salinity from CYGNSS: Algorithm and test in the Yellow River Delta," *Geoderma*, vol. 432, 2023, Art. no. 116417.

[82] M. Piles, G. Camps-Valls, D. Chaparro, D. Entekhabi, A. G. Konings, and T. Jagdhuber, "Remote sensing of vegetation dynamics in agro-ecosystems using smap vegetation optical depth and optical vegetation indices," in *Proc. IEEE Int. Geosci. Remote Sens. Symp.*, 2017, pp. 4346–4349.

[83] N. Rodriguez-Alvarez, S. Misra, and M. Morris, "The polarimetric sensitivity of SMAP-reflectometry signals to crop growth in the U.S. corn belt," *Remote Sens.*, vol. 12, no. 6, 2020, Art. no. 1007.

[84] H. Carreno-Luengo, G. Luzi, and M. Crosetto, "Above-ground biomass retrieval over tropical forests: A novel GNSS-R approach with CyGNSS," *Remote Sens.*, vol. 12, no. 9, May 2020, Art. no. 1368.

[85] E. Santi et al., "Remote sensing of forest biomass using GNSS reflectometry," *IEEE J. Sel. Topics Appl. Earth Observ. Remote Sens.*, vol. 13, pp. 2351–2368, 2020.

[86] F. Chen, F. Guo, L. Liu, and Y. Nan, "An improved method for pan-tropical above-ground biomass and canopy height retrieval using CYGNSS," *Remote Sens.*, vol. 13, no. 13, 2021, Art. no. 2491.

[87] N. Rodriguez-Alvarez, J. F. Munoz-Martin, X. Bosch-Lluis, K. Oudrhiri, D. Entekhabi, and A. Colliander, "The first polarimetric GNSS-reflectometer instrument in space improves the SMAP mission's sensitivity over densely vegetated areas," *Sci. Rep.*, vol. 13, no. 1, Mar. 2023, Art. no. 3722.

[88] J. F. Munoz-Martin, N. Rodriguez-Alvarez, X. Bosch-Lluis, and K. Oudrhiri, "Analysis of polarimetric GNSS-R Stokes parameters of the Earth's land surface," *Remote Sens. Environ.*, vol. 287, 2023, Art. no. 113491.

[89] G. Pilikos, M. P. Clarizia, and N. Floury, "Biomass estimation with GNSS reflectometry using a deep learning retrieval model," *Remote Sens.*, vol. 16, no. 7, 2024, Art. no. 1125.

[90] E. Santi et al., "Forest biomass estimate on local and global scales through GNSS reflectometry techniques," in *Proc. IEEE Int. Geosci. Remote Sens. Symp.*, 2019, pp. 8680–8683.

[91] F. Chen, L. Liu, F. Guo, and L. Huang, "A new vegetation observable derived from spaceborne GNSS-R and its application to vegetation water content retrieval," *Remote Sens.*, vol. 16, no. 5, 2024, Art. no. 931.

[92] X. Wu et al., "First measurement of soil freeze/thaw cycles in the tibetan plateau using CYGNSS GNSS-R data," *Remote Sens.*, vol. 12, no. 15, 2020, Art. no. 2361.

[93] L. Zhang, F. Ren, H. Li, D. Cheng, and B. Sun, "The influence mechanism of freeze-thaw on soil erosion: A review," *Water*, vol. 13, no. 8, 2021, Art. no. 1010.

[94] X. Wu and S. Jin, "Can we monitor the bare soil freeze-thaw process using GNSS-R?: A simulation study," in *Earth Observing Missions and Sensors: Development, Implementation, and Characterization III*, vol. 9264. Bellingham, WA, USA: SPIE, 2014, pp. 105–110.

[95] C. Chew et al., "SMAP radar receiver measures land surface freeze/thaw state through capture of forward-scattered L-band signals," *Remote Sens. Environ.*, vol. 198, pp. 333–344, 2017.

[96] N. Rodriguez-Alvarez and E. Podest, "Characterization of the land surface freeze/thaw state with SMAP-reflectometry (SMAP-R)," in *Proc. IEEE Int. Geosci. Remote Sens. Symp.*, 2019, pp. 4024–4027.

[97] D. Comite, L. Cenci, A. Colliander, and N. Pierdicca, "Monitoring freeze-thaw state by means of GNSS reflectometry: An analysis of TechDemoSat-1 data," *IEEE J. Sel. Topics Appl. Earth Observ. Remote Sens.*, vol. 13, pp. 2996–3005, 2020.

[98] K. Rautiainen, D. Comite, J. Cohen, E. Cardellach, M. Unwin, and N. Pierdicca, "Freeze–thaw detection over high-latitude regions by means of GNSS-R data," *IEEE Trans. Geosci. Remote Sens.*, vol. 60, 2022, Art. no. 4302713.

[99] H. Carreno-Luengo and C. S. Ruf, "Retrieving freeze/thaw surface state from CYGNSS measurements," *IEEE Trans. Geosci. Remote Sens.*, vol. 60, 2022, Art. no. 4302313.

[100] H. Carreno-Luengo and C. S. Ruf, "Triggering freeze/thaw surface state monitoring from high inclination orbit GNSS-R missions: A CYGNSS-based study," in *Proc. IEEE Int. Geosci. Remote Sens. Symp.*, 2022, pp. 7632–7635.

[101] H. Carreno-Luengo and C. S. Ruf, "Mapping freezing and thawing surface state periods with the CYGNSS based F/T seasonal threshold algorithm," *IEEE J. Sel. Topics Appl. Earth Observ. Remote Sens.*, vol. 15, pp. 9943–9952, 2022.

[102] W. Yang, F. Guo, X. Zhang, T. Xu, N. Wang, and L. Jing, "Daily landscape freeze/thaw state detection using spaceborne GNSS-R data in Qinghai–Tibet Plateau," *IEEE Trans. Geosci. Remote Sens.*, vol. 61, 2023, Art. no. 4302409.

[103] W. Yang, F. Guo, X. Zhang, Z. Zhang, and Y. Zhu, "High temporal resolution quasi-global landscape soil freeze–thaw map from spaceborne GNSS-R technology and SMAP radiometer measurements," *Int. J. Appl. Earth Observ. Geoinf.*, vol. 128, 2024, Art. no. 103777.

[104] X. Wu, X. Ouyang, S. Wu, F. Wang, and Z. Duan, "Assessing the freeze/thaw states in arctic circle using Fengyun-3E GNOS-R: An initial demonstration and analysis," *IEEE J. Sel. Topics Appl. Earth Observ. Remote Sens.*, vol. 17, pp. 274–281, 2024.

[105] R. Imam, M. Pini, G. Marucco, F. Dominici, and F. Dovis, "Data from GNSS-based passive radar to support flood monitoring operations," in *Proc. Int. Conf. Localization GNSS*, 2019, pp. 1–7.

[106] K. Yu et al., "Spaceborne GNSS reflectometry," *Remote Sens.*, vol. 14, no. 7, 2022, Art. no. 1605.

[107] J. Beckheinrich, G. Beyerle, S. Schoen, H. Apel, M. Semmling, and J. Wickert, "WISDOM: GNSS-R based flood monitoring," in *Proc. Workshop Reflectometry Using GNSS Other Signals Opportunity (GNSS+ R)*, 2012, pp. 1–6.

[108] C. C. Chew, R. Shah, C. Zuffada, and A. J. Mannucci, "Wetland mapping and measurement of flood inundated area using ground-reflected GNSS signals in a bistatic radar system," in *Proc. IEEE Int. Geosci. Remote Sens. Symp.*, 2016, pp. 7184–7187.

[109] J. Beckheinrich et al., "Innovative remote sensing: Flood monitoring using GNSS reflectometry," in *Proc. EGU Gen. Assem. Conf. Abstr.*, 2014, Paper 9949.

[110] C. Chew and E. Small, "Estimating inundation extent using CYGNSS data: A conceptual modeling study," *Remote Sens. Environ.*, vol. 246, 2020, Art. no. 111869.

[111] B. Wilson-Downs, A. O'Brien, and C. Zuffada, "Retrieval of dynamic changes of surface water extent from sparse GNSS-R measurements using a model-driven approach," in *Proc. IEEE Int. Geosci. Remote Sens. Symp.*, 2022, pp. 4407–4410.

[112] D. Song, Q. Zhang, B. Wang, C. Yin, and J. Xia, "A novel dual-branch neural network model for flood monitoring in South Asia based on CYGNSS data," *Remote Sens.*, vol. 14, no. 20, 2022, Art. no. 5129.

[113] N. Rodriguez-Alvarez, E. Podest, K. Jensen, and K. C. McDonald, "Classifying inundation in a tropical wetlands complex with GNSS-R," *Remote Sens.*, vol. 11, no. 9, 2019, Art. no. 1053.

[114] P. Ghasemigoudarzi, W. Huang, O. De Silva, Q. Yan, and D. T. Power, "Flash flood detection from CYGNSS data using the RUSBoost algorithm," *IEEE Access*, vol. 8, pp. 171864–171881, 2020.

[115] P. D. T. Setti, S. Tabibi, and T. Van Dam, "CYGNSS GNSS-R data for inundation monitoring in the Brazilian Pantanal Wetland," in *Proc. IEEE Int. Geosci. Remote Sens. Symp.*, 2022, pp. 5531–5534.

[116] C. Chew, E. Small, and H. Huelsing, "Flooding and inundation maps using interpolated CYGNSS reflectivity observations," *Remote Sens. Environ.*, vol. 293, 2023, Art. no. 113598.

[117] M. Rajabi, H. Nahavandchi, and M. Hoseini, "Evaluation of CYGNSS observations for flood detection and mapping during Sistan and Baluchestan torrential rain in 2020," *Water*, vol. 12, no. 7, 2020, Art. no. 2047.

[118] W. Yang et al., "Daily flood monitoring based on spaceborne GNSS-R data: A case study on Henan, China," *Remote Sens.*, vol. 13, no. 22, 2021, Art. no. 4561.

[119] S. Zhang et al., "Using cygnss data to map flood inundation during the 2021 extreme precipitation in Henan Province, China," *Remote Sens.*, vol. 13, no. 24, 2021, Art. no. 5181.

[120] B. Downs, A. J. Kettner, B. D. Chapman, G. R. Brakenridge, A. J. O'Brien, and C. Zuffada, "Assessing the relative performance of GNSS-R flood extent observations: Case study in South Sudan," *IEEE Trans. Geosci. Remote Sens.*, vol. 61, 2023, Art. no. 4201213.

[121] T. Yang, Z. Sun, and L. Jiang, "A novel index for daily flood inundation retrieval from CYGNSS measurements," *Remote Sens.*, vol. 15, no. 2, 2023, Art. no. 524.

[122] H. Wei, T. Yu, J. Tu, and F. Ke, "Detection and evaluation of flood inundation using CYGNSS data during extreme precipitation in 2022 in Guangdong Province, China," *Remote Sens.*, vol. 15, no. 2, 2023, Art. no. 297.

[123] W. Wan et al., "Using CYGNSS data to monitor China's flood inundation during typhoon and extreme precipitation events in 2017," *Remote Sens.*, vol. 11, no. 7, 2019, Art. no. 854.

[124] S. L. K. Unnithan, B. Biswal, and C. Rüdiger, "Flood inundation mapping by combining GNSS-R signals with topographical information," *Remote Sens.*, vol. 12, no. 18, 2020, Art. no. 3026.

[125] B. Liu et al., "Statistical analysis of CyGNSS speckle and its applications to surface water mapping," *IEEE Trans. Geosci. Remote Sens.*, vol. 60, 2022, Art. no. 5803915.
[126] K. Jensen, K. McDonald, E. Podest, N. Rodriguez-Alvarez, V. Horna, and N. Steiner, "Assessing L-band GNSS-reflectometry and imaging radar for detecting sub-canopy inundation dynamics in a tropical wetlands complex," *Remote Sens.*, vol. 10, no. 9, 2018, Art. no. 1431.
[127] P. Zeiger et al., "SNR-based water height retrieval in rivers: Application to high amplitude asymmetric tides in the Garonne river," *Remote Sens.*, vol. 13, no. 9, 2021, Art. no. 1856.
[128] J. Wang, Y. Hu, and Z. Li, "A new coherence detection method for mapping inland water bodies using CYGNSS data," *Remote Sens.*, vol. 14, no. 13, 2022, Art. no. 3195.
[129] X. Wang, X. He, R. Xiao, M. Song, and D. Jia, "Millimeter to centimeter scale precision water-level monitoring using GNSS reflectometry: Application to the South-to-North Water Diversion Project, China," *Remote Sens. Environ.*, vol. 265, 2021, Art. no. 112645.
[130] Z. Ma et al., "Using CYGNSS and L-band radiometer observations to retrieve surface water fraction: A case study of the catastrophic flood of 2022 in Pakistan," *IEEE Trans. Geosci. Remote Sens.*, vol. 62, 2024, Art. no. 4203117.
[131] B. D. Chapman et al., "Comparison of SAR and CYGNSS surface water extent metrics," *IEEE J. Sel. Topics Appl. Earth Observ. Remote Sens.*, vol. 15, pp. 3235–3245, 2022.
[132] S. Zhang et al., "POBI interpolation algorithm for CYGNSS near real time flood detection research: A case study of extreme precipitation events in Henan, China in 2021," *Adv. Space Res.*, vol. 71, no. 6, pp. 2862–2878, 2023.
[133] W. Li, E. Cardellach, S. RibÓ, A. Rius, and B. Zhou, "First spaceborne demonstration of BeiDou-3 signals for GNSS reflectometry from CYGNSS constellation," *Chin. J. Aeronaut.*, vol. 34, no. 9, pp. 1–10, 2021.
[134] Q. Yan, S. Liu, T. Chen, S. Jin, T. Xie, and W. Huang, "Mapping surface water fraction over the pan-tropical region using CYGNSS data," *IEEE Trans. Geosci. Remote Sens.*, vol. 62, 2024, Art. no. 5800914.
[135] C. Zuffada et al., "State of the art in GNSS-R capabilities over inland waters," in *Proc. IEEE Int. Geosci. Remote Sens. Symp.*, 2021, pp. 950–953.
[136] D. E. Alsdorf, E. Rodríguez, and D. P. Lettenmaier, "Measuring surface water from space," *Rev. Geophys.*, vol. 45, no. 2, 2007, Art. no. 2006RG000197.
[137] C. Gerlein-Safdi and C. S. Ruf, "A CYGNSS-based algorithm for the detection of inland waterbodies," *Geophys. Res. Lett.*, vol. 46, no. 21, pp. 12065–12072, 2019.
[138] E. Loria, A. O'Brien, V. Zavorotny, and C. Zuffada, "Wind vector and wave height retrieval in inland waters using CYGNSS," in *Proc. IEEE Int. Geosci. Remote Sens. Symp.*, 2020, pp. 7029–7032.
[139] P. Ghasemigoudarzi, W. Huang, O. D. Silva, Q. Yan, and D. Power, "A machine learning method for inland water detection using CYGNSS data," *IEEE Geosci. Remote Sens. Lett.*, vol. 19, 2022, Art. no. 8001105.
[140] S. Kossieris, M. Asgarimehr, and J. Wickert, "Unsupervised machine learning for GNSS reflectometry inland water body detection," *Remote Sens.*, vol. 15, no. 12, 2023, Art. no. 3206.
[141] H. Carreno-Luengo, C. S. Ruf, S. Gleason, and A. Russel, "A new multiresolution CYGNSS data product for fully and partially coherent scattering," *IEEE Trans. Geosci. Remote Sens.*, vol. 61, 2023, Art. no. 4408118.
[142] V. Zavorotny, E. Loria, A. O'Brien, B. Downs, and C. Zuffada, "Investigation of coherent and incoherent scattering from lakes using CYGNSS observations," in *Proc. IEEE Int. Geosci. Remote Sens. Symp.*, 2020, pp. 5917–5920.
[143] W. Li, E. Cardellach, F. Fabra, S. Ribó, and A. Rius, "Applications of spaceborne GNSS-R over inland waters and wetlands," in *Proc. IEEE Int. Geosci. Remote Sens. Symp.*, 2019, pp. 5255–5258.
[144] M. M. Al-Khaldi et al., "Inland water body mapping using CYGNSS coherence detection," *IEEE Trans. Geosci. Remote Sens.*, vol. 59, no. 9, pp. 7385–7394, Sep. 2021.
[145] M. Morris, H. Nguyen, M. Bonnema, C. H. David, and E. Loria, "A probabilistic approach to mapping inland water bodies with GNSS-R," in *Proc. IEEE Int. Geosci. Remote Sens. Symp.*, 2022, pp. 4399–4402.
[146] Q. Yan et al., "Inland water mapping based on GA-LinkNet from CyGNSS data," *IEEE Geosci. Remote Sens. Lett.*, vol. 20, 2023, Art. no. 1500305.
[147] S. Bhattacharya, Y. Wang, and Y. J. Morton, "Detection of surface water using spire grazing-angle GNSS-R data," in *Proc. IEEE Int. Geosci. Remote Sens. Symp.*, 2023, pp. 2719–2722.
[148] J. Zhang, Y. J. Morton, Y. Wang, and C. J. Roesler, "Mapping surface water extents using high-rate coherent spaceborne GNSS-R measurements," *IEEE Trans. Geosci. Remote Sens.*, vol. 60, 2022, Art. no. 4211115.
[149] M. Scott, C. Chew, Y. Wang, C. Roesler, and Y. J. Morton, "On the relationship between the GNSS-R signal SNR and coherency with surface water: A case study over lake okeechobee," in *Proc. IEEE Int. Geosci. Remote Sens. Symp.*, 2023, pp. 3345–3348.
[150] E. Loria et al., "Comparison of GNSS-R coherent reflection detection algorithms using simulated and measured CYGNSS data," *IEEE Trans. Geosci. Remote Sens.*, vol. 61, 2023, Art. no. 5105216.
[151] H. Carreno-Luengo, C. S. Ruf, S. Gleason, and A. Russel, "Detection of inland water bodies under dense biomass by CYGNSS," *Remote Sens. Environ.*, vol. 301, 2024, Art. no. 113896.
[152] H. Carreno-Luengo et al., "In-orbit real time inland water detection by a future spaceborne GNSS-R receiver," in *Proc. IEEE Int. Geosci. Remote Sens. Symp.*, 2023, pp. 3724–3725.
[153] M. Chang, P. Li, Y. Hu, Y. Sun, H. Wang, and Z. Li, "A new algorithm for mapping large inland water bodies using CYGNSS," *Int. J. Remote Sens.*, vol. 45, no. 5, pp. 1522–1538, 2024.
[154] P. T. Setti and S. Tabibi, "Spaceborne GNSS-reflectometry for surface water mapping in the Amazon basin," *IEEE J. Sel. Topics Appl. Earth Observ. Remote Sens.*, vol. 17, pp. 6658–6670, 2024.
[155] Y. Zhang, Z. Yan, S. Yang, W. Meng, Y. Han, and Z. Hong, "Feasibility study on Qinghai lake boundary detection using CYGNSS raw IF data," *IEEE J. Sel. Topics Appl. Earth Observ. Remote Sens.*, vol. 17, pp. 8397–8408, 2024.
[156] G. Pavur, H. Kim, B. Fang, and V. Lakshmi, "Spatial comparison of inland water observations from CYGNSS, MODIS, Landsat, and commercial satellite imagery," *Geosci. Lett.*, vol. 11, no. 1, 2024, Art. no. 12.
[157] S. V. Nghiem et al., "Wetland monitoring with global navigation satellite system reflectometry," *Earth Space Sci.*, vol. 4, no. 1, pp. 16–39, Jan. 2017.
[158] C. Zuffada, C. Chew, and S. V. Nghiem, "Global navigation satellite system reflectometry (GNSS-R) algorithms for wetland observations," in *Proc. IEEE Int. Geosci. Remote Sens. Symp.*, 2017, pp. 1126–1129.
[159] W. Li, E. Cardellach, F. Fabra, S. Ribó, and A. Rius, "Lake level and surface topography measured with spaceborne GNSS-reflectometry from CYGNSS mission: Example for the Lake Qinghai," *Geophysical Res. Lett.*, vol. 45, no. 24, pp. 13 332–13 341, 2018.
[160] C. S. Ruf et al., "A new paradigm in earth environmental monitoring with the CYGNSS small satellite constellation," *Sci. Rep.*, vol. 8, no. 1, Jun. 2018, Art. no. 8782.
[161] M. Morris, C. Chew, J. T. Reager, R. Shah, and C. Zuffada, "A novel approach to monitoring wetland dynamics using CYGNSS: Everglades case study," *Remote Sens. Environ.*, vol. 233, 2019, Art. no. 111417.
[162] H. Arai et al., "Quality control of CyGNSS reflectivity for robust spatiotemporal detection of tropical wetlands," *Remote Sens.*, vol. 14, no. 22, 2022, Art. no. 5903.
[163] P. Zeiger, F. Frappart, J. Darrozes, C. Prigent, C. Jiménez, and L. Bourrel, "Weekly mapping of surface water extent in the intertropical wetlands using spaceborne GNSS reflectometry," *J. Hydrol.*, vol. 626, 2023, Art. no. 130305.
[164] B. Downs, A. O'Brien, M. Morris, and C. Zuffada, "Water depth retrieval in the everglades using CYGNSS," in *Proc. IEEE Int. Geosci. Remote Sens. Symp.*, 2021, pp. 5903–5906.
[165] B. Downs, A. O'Brien, M. Morris, V. Zavorotny, and C. Zuffada, "Using GNSS reflectometry measurements over the everglades to identify variations in wetland inundation extent beneath vegetation," 2021. [Online]. Available: https://doi.org/10.1002/essoar.10506211.1
[166] C. Zuffada et al., "An assessment of the capabilities of GNSS reflectometry for dynamic monitoring of wetlands and inundations," *Advance*, 2020. [Online]. Available: https://doi.org/10.1002/essoar.10502084.1
[167] E. Santi, M. P. Clarizia, D. Comite, L. Dente, L. Guerriero, and N. Pierdicca, "On the use of GNSS reflectometry for detecting fire disturbances in forests: A case study in Angola," in *Proc. IEEE Int. Geosci. Remote Sens. Symp.*, 2021, pp. 6024–6027.
[168] E. Santi, M. P. Clarizia, D. Comite, L. Dente, L. Guerriero, and N. Pierdicca, "Detecting fire disturbances in forests by using GNSS reflectometry and machine learning: A case study in Angola," *Remote Sens. Environ.*, vol. 270, 2022, Art. no. 112878.
[169] E. Santi et al., "Machine learning applications for classification and retrieval of surface parameters from GNSS-R," in *Proc. IEEE Int. Geosci. Remote Sens. Symp.*, 2023, pp. 1174–1177.

[170] H. Carreno-Luengo, G. Luzi, and M. Crosetto, "First evaluation of topography on GNSS-R: An empirical study based on a digital elevation model," *Remote Sens*, vol. 11, no. 21, 2019, Art. no. 2556.
[171] H. Carreno-Luengo, G. Luzi, and M. Crosetto, "Effects of rough topography in GNSS-R: A parametric study based on a digital elevation model," in *Proc. IEEE Int. Geosci. Remote Sens. Symp.*, 2019, pp. 8663–8666.
[172] D. Stilla, M. Zribi, N. Pierdicca, N. Baghdadi, and M. Huc, "Desert roughness retrieval using CYGNSS GNSS-R data," *Remote Sens.*, vol. 12, no. 4, 2020, Art. no. 743.
[173] L. Dente, L. Guerriero, D. Comite, and N. Pierdicca, "Space-borne GNSS-R signal over a complex topography: Modeling and validation," *IEEE J. Sel. Topics Appl. Earth Observ. Remote Sens.*, vol. 13, pp. 1218–1233, 2020.
[174] M. Song et al., "Investigation on geometry computation of spaceborne GNSS-R altimetry over topography: Modeling and validation," *Remote Sens.*, vol. 14, no. 9, 2022, Art. no. 2105.
[175] J. D. Campbell, A. Melebari, and M. Moghaddam, "Modeling the effects of topography on delay-Doppler maps," *IEEE J. Sel. Topics Appl. Earth Observ. Remote Sens.*, vol. 13, pp. 1740–1751, 2020.
[176] Y. Wang and Y. Morton, "Coherent and semi-coherent spaceborne GNSS-R for land surface altimetry applications," in *Proc. 33rd Int. Tech. Meeting Satell. Div. Inst. Navigation*, 2020, pp. 3901–3908.
[177] J. Zhang and Y. J. Morton, "Inland water body surface height retrievals using CYGNSS delay Doppler maps," *IEEE Trans. Geosci. Remote Sens.*, vol. 61, 2023, Art. no. 4209316.
[178] L. Xu, W. Wan, X. Chen, S. Zhu, B. Liu, and Y. Hong, "Spaceborne GNSS-R observation of global lake level: First results from the TechDemoSat-1 mission," *Remote Sens.*, vol. 11, no. 12, 2019, Art. no. 1438.
[179] C. Yanez et al., "Lake water level estimation from grazing GNSS-reflectometry and satellite radar altimetry over the Great Lakes," *IEEE Geosci. Remote Sens. Lett.*, vol. 21, 2024, Art. no. 1503005.
[180] Y. Wang and Y. J. Morton, "Observation of the mississippi river surface gradients from spire's GNSS-R CubeSats," in *Proc. IEEE Int. Geosci. Remote Sens. Symp.*, 2022, pp. 4403–4406.
[181] Y. Wang and Y. J. Morton, "River slope observation from spaceborne GNSS-R carrier phase measurements: A case study," *IEEE Geosci. Remote Sens. Lett.*, vol. 19, 2022, Art. no. 1503105.
[182] A. Warnock and C. Ruf, "Response to variations in river flowrate by a spaceborne GNSS-R river width estimator," *Remote Sens.*, vol. 11, no. 20, 2019, Art. no. 2450.
[183] A. Warnock, C. S. Ruf, and A. L. Knoll, "Characterization of river width measurement capability by space borne GNSS-reflectometry," *Remote Sens.*, vol. 16, no. 8, 2024, Art. no. 1446.
[184] Y. Ghiasi, C. R. Duguay, J. Murfitt, M. Asgarimehr, and Y. Wu, "Potential of GNSS-R for the monitoring of lake ice phenology," *IEEE J. Sel. Topics Appl. Earth Observ. Remote Sens.*, vol. 17, pp. 660–673, 2024.
[185] E. Loria, A. O'Brien, V. Zavorotny, and C. Zuffada, "Towards wind vector and wave height retrievals over inland waters using CYGNSS," *Earth Space Sci.*, vol. 8, no. 7, 2021, Art. no. e2020EA001506.
[186] J. V. Fayne and M. Al-Khaldi, "Passive L-band GNSS-R and active C-and ka-band radar inland water wind speeds," in *Proc. United States Nat. Committee URSI Nat. Radio Sci. Meeting*, 2024, p. 178.
[187] N. J. Brendle, S. K. Chan, G. Hajj, M. M. Al-Khaldi, and J. T. Johnson, "Reservoir water level monitoring using CYGNSS's level-1 observations," *IEEE J. Sel. Topics Appl. Earth Observ. Remote Sens.*, vol. 17, pp. 9090–9098, 2024.
[188] J. V. Fayne, "Inland water inundation extent and wind speeds from passive L-band GNSS-R and active C- and Ka-band radar," in *Proc. Int. Conf. Electromagn. Adv. Appl. (ICEAA)*, 2023, p. 574.
[189] Y. Liu, R. Min, H. Du, and W. Guo, "Assessing the performance of GNSS-R observations in drought monitoring: A case study in Jiangxi and Hunan, China," *Geocarto Int.*, vol. 39, no. 1, 2024, Art. no. 2333351.
[190] K. Edokossi, S. Jin, U. Mazhar, I. Molina, A. Calabia, and I. Ullah, "Monitoring the drought in Southern Africa from space-borne GNSS-R and SMAP data," *Natural Hazards*, vol. 120, pp. 7947–7967, 2024.
[191] Q. Yan et al., "Improving CyGNSS-based land remote sensing: Track-wise data calibration schemes," *Remote Sens.*, vol. 13, no. 14, 2021, Art. no. 2844.
[192] Y. Zhang, Y. Wang, S. Zhou, W. Meng, Y. Han, and S. Yang, "Feasibility study of spaceborne GNSS-R detection of algal blooms in Taihu Lake," *J. Beijing Univ. Aeronaut. Astronaut.*, vol. 13, pp. 1–14, 2022.
[193] Q. Yan and D. Wang, "Spatiotemporal response of CYGNSS signals to precipitation and analysis of driving factors," *Geomatics Inf. Sci. Wuhan Univ.*, vol. 49, no. 1, pp. 109–121, 2024.
[194] Y. Wang, "Grazing-angle GNSS-R for the determination of tropospheric delay and water vapor content," in *Proc. 36th Int. Tech. Meeting Satell. Div. Inst. Navigation*, 2023, pp. 3227–3232.
[195] Y. Wang, "Troposphere sensing using grazing-angle GNSS-R measurement from LEO satellites," *Geophys. Res. Lett.*, vol. 50, no. 24, 2023, Art. no. e2023GL106249.
[196] Q. Yan, S. Gong, S. Jin, W. Huang, and C. Zhang, "Near real-time soil moisture in China retrieved from CyGNSS reflectivity," *IEEE Geosci. Remote Sens. Lett.*, vol. 19, 2022, Art. no. 8004205.
[197] N. Rodriguez-Alvarez, S. Misra, and M. Morris, "Sensitivity analysis of SMAP-reflectometry (SMAP-R) signals to vegetation water content," in *Proc. IEEE Int. Geosci. Remote Sens. Symp.*, 2019, pp. 7395–7398.
[198] N. Rodriguez-Alvarez, S. Misra, E. Podest, M. Morris, and X. Bosch-Lluis, "The use of SMAP-reflectometry in science applications: Calibration and capabilities," *Remote Sens.*, vol. 11, no. 20, 2019, Art. no. 2442.
[199] N. Rodriguez-Alvarez, J. F. Munoz-Martin, X. Bosch-Lluis, and K. Oudrhiri, "Introduction to the new SMAP-reflectometry (SMAP-R) dataset: Status and science capabilities," in *Proc. IEEE Int. Geosci. Remote Sens. Symp.*, 2022, pp. 7624–7627.
[200] J. F. Munoz-Martin, N. Rodriguez-Alvarez, X. Bosch-Lluis, and K. Oudrhiri, "Initial evaluation of SMAP-R polarimetry over land," in *Proc. IEEE Int. Geosci. Remote Sens. Symp.*, 2022, pp. 5788–5791.
[201] H. Carreno-Luengo, A. Amèzaga, D. Vidal, R. Olivé, J. F. Munoz, and A. Camps, "First polarimetric GNSS-R measurements from a stratospheric flight over boreal forests," *Remote Sens.*, vol. 7, no. 10, pp. 13120–13138, 2015.

Jinwei Bu (Member, IEEE) received the B.S. degree in surveying and mapping engineering and the M.S. degree in geodesy and surveying engineering from the Kunming University of Science and Technology, Kunming, China, in 2016 and 2018, respectively, and the Ph.D. degree in geodesy and surveying engineering from the School of Environmental Science and Spatial Informatics, China University of Mining and Technology, Xuzhou, China, in 2022.

He was a Visiting Ph.D. student with the Department of Signal Theory and Communications, Universitat Politècnica de Catalunya, Barcelona, Spain, for 12 months, i.e., from 2021 to 2022. He is currently a Master Supervisor with the Faculty of Land Resource Engineering, Kunming University of Science and Technology, Kunming. He has authored or coauthored more than 50 refereed journal articles. He serves as a reviewer for more than ten international journals, such as IEEE TRANSACTIONS ON GEOSCIENCE AND REMOTE SENSING, *GPS Solutions*, *IEEE Internet of Things Journal*, *Ocean Engineering*, *Remote Sensing*, *Measurement*, *Advances in Space Research*, and *Measurement Science and Technology*. His research interests include global navigation satellite systems (GNSS) reflectometry, GNSS atmospheric remote sensing, GNSS precision positioning, and machine/deep learning.

Qiulan Wang is currently working toward the B.Sc. degree in geographic information science with the Faculty of Land Resources Engineering, Kunming University of Science and Technology, Kunming, China.

Her research interest focuses on global navigation satellite systems reflectometry.

Ziyi Wang is currently working toward the B.Sc. degree in surveying and mapping engineering with the Faculty of Land Resources Engineering, Kunming University of Science and Technology, Kunming, China.

His research interest focuses on global navigation satellite systems reflectometry.

Shaoqiang Fan is currently working toward the B.Sc. degree in surveying and mapping engineering with the Faculty of Land Resources Engineering, Kunming University of Science and Technology, Kunming, China.

His research interest focuses on global navigation satellite systems reflectometry.

Xinyu Liu received the bachelor's degree in engineering from the City College of Kunming University of Science and Technology, Kunming, China, in 2023. She is currently working toward the master's degree in surveying and mapping engineering with the Faculty of Land Resource Engineering, Kunming University of Science and Technology.

Her research interest focuses on global navigation satellite systems reflectometry (GNSS-R).

Xiaoqing Zuo received the M.S. degree from the Kunming University of Science and Technology, Kunming, China, in 2001, and the Ph.D. degree from Wuhan University, Wuhan, China, in 2004, both in geographic information science.

He is currently a Professor with the Kunming University of Science and Technology. His main research interests include data mining, InSAR theory and technology, and remote sensing image processing and analysis.

Dr. Zuo was named Yunnan Young and Middle-Aged Academic and Technical Leaders Reserve Talent. He is also the Deputy Director of the GIS Professional Committee of the Yunnan Provincial Surveying and Mapping Society.